Molecular Therapy
Oncolytics
Original Article

Spatiotemporal analysis of induced neural stem cell therapy to overcome advanced glioblastoma recurrence

Andrew B. Satterlee,[1] Denise E. Dunn,[2] Alain Valdivia,[1] Daniel Malawsky,[3] Andrew Buckley,[1] Timothy Gershon,[3,4,5] Scott Floyd,[2] and Shawn Hingtgen[1,5]

[1]Division of Pharmacoengineering and Molecular Pharmaceutics, UNC Eshelman School of Pharmacy, University of North Carolina at Chapel Hill, Chapel Hill, NC 27599, USA; [2]Department of Radiation Oncology, Duke University Medical Center, Durham, NC 27704, USA; [3]Department of Neurology, University of North Carolina School of Medicine, Chapel Hill, NC 27599, USA; [4]UNC Neuroscience Center, University of North Carolina School of Medicine, Chapel Hill, NC 27599, USA; [5]Lineberger Comprehensive Cancer Center, University of North Carolina School of Medicine, Chapel Hill, NC 27599, USA

Genetically engineered neural stem cells (NSCs) are a promising therapy for the highly aggressive brain cancer glioblastoma (GBM); however, treatment durability remains a major challenge. We sought to define the events that contribute to dynamic adaptation of GBM during treatment with human skin-derived induced NSCs releasing the pro-apoptotic agent TRAIL (iNSC-TRAIL) and develop strategies that convert initial tumor kill into sustained GBM suppression. *In vivo* and *ex vivo* analysis before, during, and after treatment revealed significant shifts in tumor transcriptome and spatial distribution as the tumors adapted to treatment. To address this, we designed iNSC delivery strategies that increased spatiotemporal TRAIL coverage and significantly decreased GBM volume throughout the brain, reducing tumor burden 100-fold as quantified in live *ex vivo* brain slices. The varying impact of different strategies on treatment durability and median survival of both solid and invasive tumors provides important guidance for optimizing iNSC therapy.

INTRODUCTION

Glioblastoma (GBM) is a highly aggressive form of brain cancer, often composed of one or more solid masses and diffuse cells that invade throughout the brain. Invasive cancer cells evade surgical resection and systemic chemotherapy regimens often fail to eliminate the remaining cancer, leading to dismal survival rates.[1–3] Therapies that seek out the disseminated GBM cells behind the blood-brain barrier are needed to prevent recurrence in patients, and the unique tumor-homing capacity of genetically engineered neural stem cells (NSCs) allows them to deliver anti-cancer gene products directly to local and invasive GBM foci.[4–7] These cells can significantly reduce human GBM xenografts and suppress post-surgical recurrence.[6,8–14] NSC therapy for post-surgical GBM recently entered human patient testing on the strength of their pre-clinical tumor kill.

To create an autologous NSC source where the potential to avoid immune rejection could allow improved homing and tumor kill, we recently discovered that transdifferentiation, a process that transforms somatic cells into other adult cell types, creates tumor-homing drug carriers capable of regressing GBM xenografts.[15–17] Using a defined set of transcription factors, we "flipped" human and mouse fibroblasts into induced NSCs (iNSCs) that can home to GBM cells with the same velocity as brain-derived NSCs and migrate through the brain, tracking invasive human GBM cells. *In vitro*, genetically engineered iNSCs release the pro-apoptotic agent TRAIL (iNSC-TRAIL) at levels equal to cortical-derived NSCs and effectively kill co-cultured GBM cells. In orthotopic xenograft models, iNSC-TRAIL therapy can reduce solid human GBM and extend median survival compared with untreated control from 39 to 60 days in mice bearing diffuse patient-derived GBMs. We have also shown that iNSC-TRAIL therapy is effective in treating heterogeneous GBM tumors *in vivo* and have quantified consequences of TRAIL-resistant tumor sub-populations.[18] Despite the promise of this approach, initial reductions in GBM volumes are often not well maintained. Treatment durability remains a major limitation to this promising strategy.

It is likely that GBM evades iNSC therapy through both failure of drug delivery and adaptive tumor behavior. One of the studies described above shows that even when 10-fold excess of tumoricidal mouse iNSC-TRAIL was co-implanted with GBM cells, a significant initial reduction in tumor volumes was detected. However, confocal microscopy on brain sections revealed the presence of residual mCherry + GBM foci in the brain 14 days after treatment. Tumoricidal iNSC-TRAIL therapy suppressed re-growth of these solid tumor foci through day 28, and re-growth of highly invasive GBM8 xenografts was minimal through day 33. Yet, tumor suppression was lost in

Received 13 December 2021; accepted 1 June 2022;
https://doi.org/10.1016/j.omto.2022.06.004.

Correspondence: Shawn Hingtgen, 4212 Marsico Hall, 125 Mason Farm Road, Chapel Hill, NC 27599, USA.
E-mail: hingtgen@email.unc.edu
Correspondence: Andrew Satterlee, 4229J Marsico Hall, 125 Mason Farm Road, Chapel Hill, NC 27599, USA.
E-mail: satterle@email.unc.edu

both models, and animals died from re-growth of both solid and invasive tumors. The precise time point when accelerated re-growth begins and how the onset of treatment failure correlates with the levels of iNSC loss, iNSC migration, or tumor adaption throughout this period of GBM recurrence is virtually unexplored.

Robust models of aggressive GBM that recapitulate the late-stage presentation of the human disease are needed to elucidate these important mechanisms of tumor recurrence in the context of iNSC therapy. Herein, we expand our exploration of GBM resistance and recurrence by combining our unique *in vivo* late-stage GBM model and *ex vivo* organotypic brain slice assays with tumor-homing iNSC therapy and next-gen mRNA sequencing to investigate the events contributing to loss of GBM response after iNSC treatment. This information allowed us to strategically modulate the implant site and dosing frequency of iNSC therapy to achieve broader killing and knockdown of orthotopic human GBM by using patient-derived xenografts in immunodeficient mice. A central goal of these studies is to understand the adaptation of GBM to iNSC-delivered drugs, so we purposefully chose to use iNSCs that secrete a well-characterized therapeutic molecule—TRAIL—as it is ideal to accomplish our focused therapeutic assessments. In this way, we intend to take critical steps toward generating a responsive iNSC strategy that can achieve lasting suppression of GBM and be easily translatable for use in patients.

RESULTS

Determining the durability and pattern of GBM re-growth after NSC therapy

Although many studies focus on initial eradication of a focal tumor, we sought to focus on a poorly studied aspect of NSC therapy: tumor recurrence in late-stage, invasive GBM. Understanding this bleak, relatively unstudied, and commonly encountered state of GBM is essential to define mechanisms limiting treatment efficacy and durability. A model of human GBM previously established by us[18] was modified and used to begin elucidating mechanisms behind treatment resistance. This interesting model initially contained two limited-passage cell populations derived from the same human patient biopsy, which were mixed and implanted orthotopically into nude mouse brains. Our previous results showed interactions between these two cell lines, termed G-EF and G-FBS, which fostered the growth of a dense, solid mass and an extensive invasive component. Here, we allowed every patient-matched tumor to grow for 28 days before initiating treatment, generating a tumor model with widespread invasion representative of aggressive, late-stage GBM. As the tumors grow, the G-EF cells vastly outgrow the less tumorigenic G-FBS cells, resulting in tumors that are entirely composed of G-EF cells (verified by PCR; Figure S1).

To begin, we generated late-stage patient-matched tumors in the right cranial hemispheres of nude mice and treated them with a single dose of 200,000 iNSC-TRAIL cells, also in the right hemisphere (we will refer to this treatment location as right hemisphere injection, or RHI). RHI treatment led to significant tumor growth inhibition as quantified by live-animal bioluminescence imaging (BLI) (Figure 1A). However, tumors eventually escaped iNSC-TRAIL therapy, with initial increases in tumor volumes detected 14–18 days post-treatment. Despite initially robust treatment efficacy, animals quickly succumbed to recurrent tumors just 27 days post-treatment, compared with 21-day survival of the untreated group (Figure 1B). To begin exploring the events driving tumor recurrence, we analyzed the distribution of tumors within representative brains from each group. In untreated animals, fluorescence microscopy of *post mortem* coronal sections reproducibly shows a large solid mass located in the top-right quadrant of the brain, invading into the left hemisphere in a clinically relevant manner[19] along the white matter tracks of the corpus collosum (Figure 1C). In contrast, tumor burden in the top-right quadrant was markedly reduced in the brains of iNSC-TRAIL-treated mice (Figure 1D). Local tumor recurrence was more diffuse and had spread into the lower-right quadrant, as shown in the representative image. Invasion into the left hemisphere also seemed to be uninterrupted by RHI treatment, a finding explored below. These data suggested that tumor invasion plays a role in GBM escape from iNSC therapy, indicating that we should explore strategies to improve the spatial distribution of therapeutic iNSCs and allow the cells to more effectively target late-stage GBM.

Exploring tumor adaptation following iNSC therapy using mRNA sequencing

Although iNSC-TRAIL treatment produced a robust anti-tumor effect, survival was only modestly increased. To gain insight into the process of recurrence and to tie our *in* vivo results to genetic tumor data, we used mRNA sequencing (RNA-seq) to analyze transcriptomic differences between solid and invasive tumor areas that were either naive to treatment or had recurred after iNSC-TRAIL treatment.

Patient-matched tumors were implanted into the right hemispheres of six mice and allowed to grow for 28 days. Three mice then received RHI treatment with 200,000 iNSC-TRAIL cells while three mice remained untreated. At the time tumor progression required euthanasia, brains were processed and frozen in optimal cutting temperature (OCT) solution. After sectioning on a cryostat, a fluorescence-guided surgical microscope was used to carefully excise distinct regions of naive or recurrent solid tumor in the right hemisphere and invasive tumor in the left hemisphere (Figure S2). We sampled and pooled the solid tumor and invasive region from four consecutive sections of each brain to generate one solid-tumor sample and one invasive-region sample from each animal.

We subjected the two samples taken from each of the six mice to RNA-seq. Initial analysis revealed that samples contained 60%–85% human reads and 10%–35% mouse reads (Figure S3), indicating a high tumor cell abundance even within recurrent and invasive tumor samples.

We used generalized principal-component analysis (PCA) to compare human transcriptome data in the four types of samples: Solid Naive tumor (S_N), Invasive Naive tumor (I_N), Solid Recurrent tumor (S_R), and Invasive Recurrent tumor (I_R). The solid and invasive regions showed high-level differences prior to treatment, as demonstrated by their distinct localizations in two-dimensional

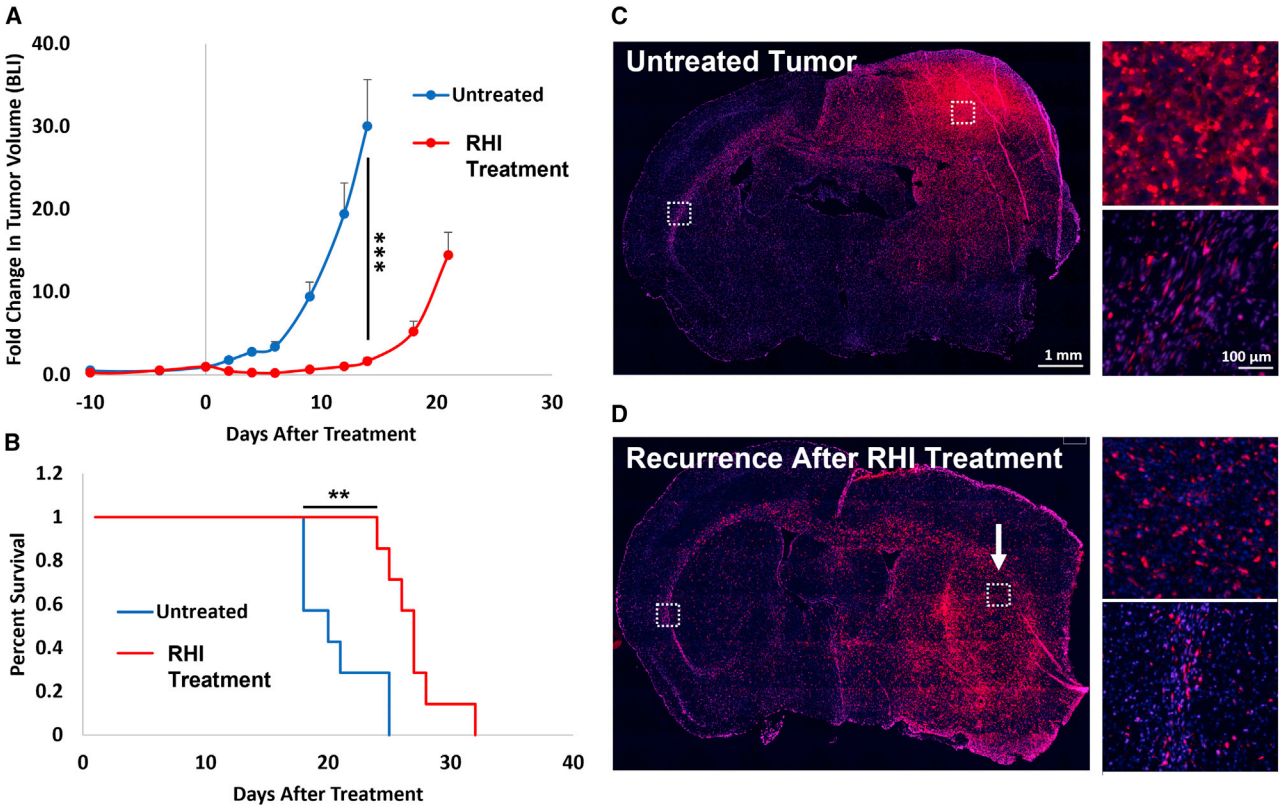

Figure 1. Recurrence after solid tumor treatment

(A) Tumor growth curves (BLI) of untreated tumors (blue line) and tumors treated with 200,000 iNSC-TRAIL via right hemisphere injection (RHI, red line). (B) Kaplan-Meier survival plot showing a significant increase in survival after RHI treatment (median survival of 21 days after treatment for untreated mice and 27 days after treatment for RHI-treated mice). (C) Representative untreated tumor at time of death. Top: high-magnification image shows solid-tumor burden. Bottom: high-magnification image shows invasive tumor cells (red) migrating across the corpus callosum. (D) Representative recurrent tumor at time of death. Top: high-magnification image shows tumor recurring near the iNSC-TRAIL implant site. Bottom: high-magnification image shows invasive tumor cells as in (C); n = 7–8 mice per group. Data expressed as mean ± SEM. **$p < 0.01$; ***$p < 0.001$.

generalized PCA space (Figure 2A). Treatment shifted both solid and invasive recurrent tumors to be less similar to naive tumors and markedly similar to each other, as demonstrated by their proximity in PCA space. Hierarchical clustering also demonstrated that recurrent solid and invasive tumors were similar to each other and different from the untreated samples of either region (Figure 2B).

We analyzed changes in individual genes in several ways. A number of genes were differentially expressed when measured in pairwise comparison within each of four different relationships: S_N versus S_R, I_N versus I_R, S_N versus I_N, and S_R versus I_R (Figure S4). These data agreed with the overall PCA analysis, showing that recurrent solid and recurrent invasive tumors were the most similar, with the fewest differentially expressed genes. We also determined the 20 overall most variable genes via unsupervised hierarchical clustering (Figure S5) as well as genes whose expression was significantly and similarly changed in all six recurrent tumor samples compared with naive and in all six invasive tumor samples compared with solid ($p < 0.001$; Figure S6).

Defining functional changes that result from differential expression of a single gene can be challenging. Gene ontology is a common strategy to overcome this issue by grouping genes based on common functional traits. We used gene ontology to more effectively understand functional trends and outcomes of overall gene expression changes, analyzing the transcriptomic changes between groups and identifying the impact of treatment on well-known signaling pathways. We referenced pathways as described in the Kyoto Encyclopedia of Genes and Genomes (KEGG) and quantified which pathways were significantly changed in each of the four different comparisons described above (Figures 2C, S7, and S8). The four plots corresponding to the four comparisons display changes in genes among 70 different pathways arranged in rows from top to bottom. The names of all 70 pathways are included with each enlarged plot in Figure S7, while the plots shown in Figure 2C should be used to view overall trends. The *size* of the circle on each row corresponds to the *number* of genes within the pathway with significantly changed expression, the *position* of each circle along the x axis corresponds to the *percentage* of genes within the pathway with significantly changed gene expression, and

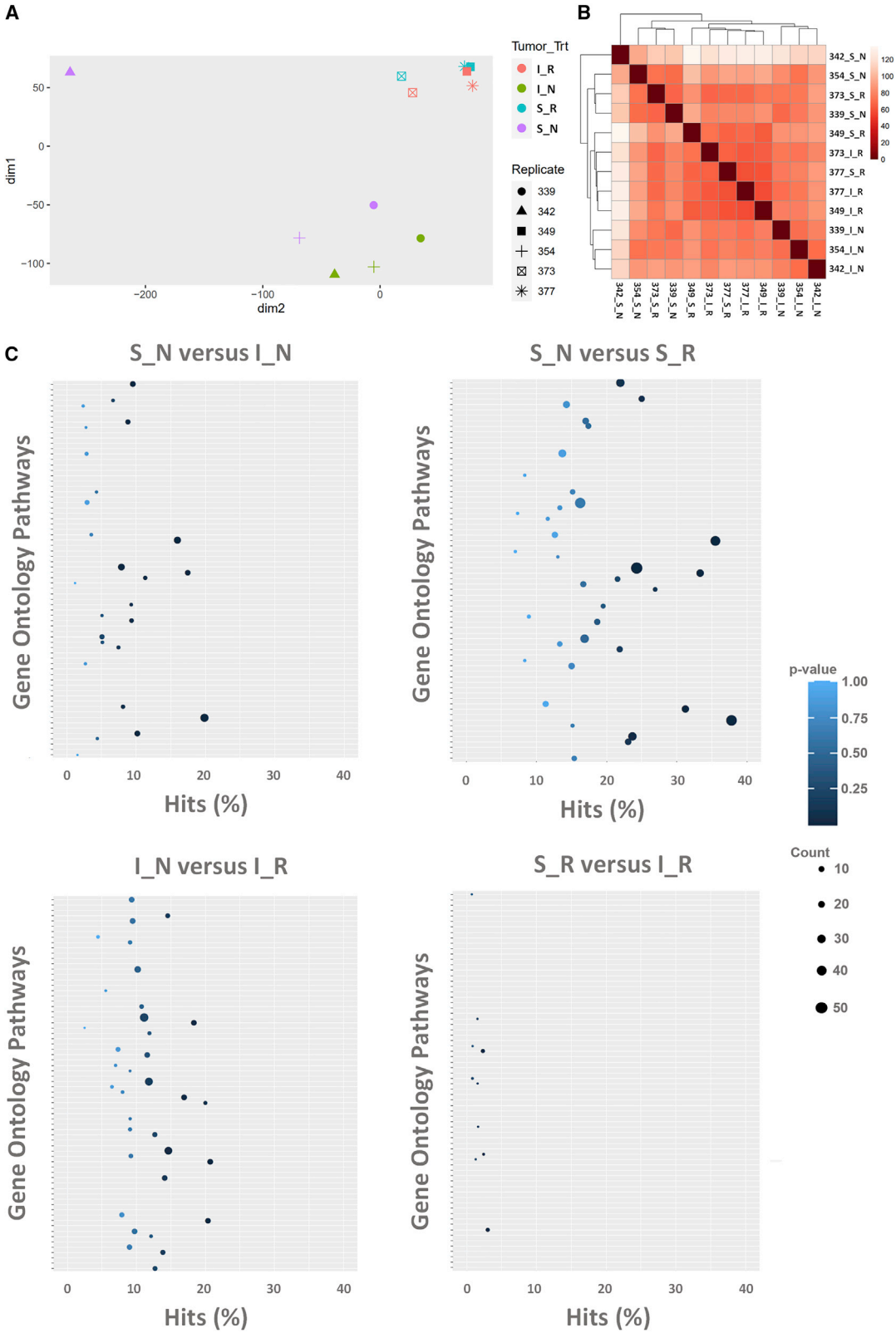

(legend on next page)

the *color* of each circle corresponds to the statistical significance of expression changes within the pathway as a whole. Pathways with more significant changes display a large, dark, right-positioned circle.

These plots mirrored the generalized PCA plot, showing that the largest changes among these 70 pathways occur between the naive solid tumor and the recurrent tumor that re-grows in its place (S_N versus S_R). In contrast, there was almost no difference between recurrent tumors in the solid and invasive regions (S_R versus I_R). Interestingly, there were fewer overall pathway changes between the naive and recurrent invasive tumor (I_N versus I_R) than between the naive and recurrent solid tumor (S_N versus S_R). This suggests that, as the naive tumor grew, the sub-population of treatment-naïve invading cells were more similar to the recurrent tumor than the non-invading sub-population. Figure S7 shows many significant changes to cancer-related signaling pathways such as MAPK, Wnt, and VEGF between S_N and S_R, but changes among these pathways were less dramatic when I_N versus I_R was compared. We saw the same trend within the calcium-signaling pathway (implicated in the progression and invasion of GBM[20,21]) which was greatly changed in S_N versus S_R but much less so in I_N versus I_R. Furthermore, this trend extended to cell motility pathways such as those regulating tight junctions and gap junctions, which were greatly modified in S_N versus S_R but less so in I_N versus I_R, affirming that the invasive naive tumor sub-population expressed a more oncogenic and mesenchymal phenotype than the naive solid tumor. This phenotype was further exacerbated in the invasive population after treatment and similarly expressed within the recurrent solid tumor. Interestingly, no comparisons revealed significant changes in the necroptosis or TNF-signaling pathways implicated in TRAIL-mediated cell death, suggesting that the recurrent tumor had not lost sensitivity to TRAIL. As described below, this finding was corroborated via *ex vivo* and *in vivo* assays.

Taken together, these data show that the invasive tumor population is distinct from the solid tumor in advance of treatment, with gene expression patterns in the invasive tumor consistent with a more migratory phenotype. Although both solid and invasive cell populations change after treatment and recurrence, the effect of treatment reduces regional variation and heterogeneity. This provides initial speculation that the cells that spatially escape treatment may re-populate both areas and suggests that strategies to broaden iNSC distribution and increase coverage of TRAIL may improve therapeutic durability and increase survival.

Distal iNSC therapy to target invasive GBM

In the clinical setting, many GBM patients present with large solid tumors with widespread microinvasion throughout the brain parenchyma that is often undetectable via MRI.[22] New strategies are being employed to increase chemotherapeutic coverage, including infusion of therapeutics directly into the lateral ventricles of the brain.[23] This intracerebroventricular (ICV) infusion route is amenable to continuous or repeated infusions through the use of an Ommaya reservoir with a catheter leading to the ventricles and is routinely used by some neuro-oncologists to treat patients with CNS cancers.[24–27]

The clinical use of ICV infusion suggests an interesting route for iNSC delivery that could allow widespread distribution of iNSCs throughout the ventricles, placing the cells closer to distant tumor foci that cannot be reached by local GBM therapy. Using our patient-matched *in vivo* model of late-stage GBM, we investigated the impact of infusing therapeutic iNSC-TRAIL cells at distal sites by delivery into the left cranial hemisphere (termed left hemisphere injection, or LHI) or into the left lateral ventricle (termed ICV [demonstrated in Figure S8]). Using serial BLI to quantify tumor progression, we found, unexpectedly, that these treatment strategies had no significant impact on overall tumor bioluminescence (Figure 3A).

As it was possible that spatially distinct tumor kill was occurring at resolutions below the detection limit of BLI, we sought to define spatial changes in GBM volume at a cellular resolution. To investigate the impact of different routes of iNSC-TRAIL injection with higher resolution, we generated living organotypic brain slices from subsets of mice at 6, 13, and 20 days after iNSC-TRAIL treatment. Using our well-established protocol, these 350-μm-thick coronally sectioned tumor-bearing brain slices were kept alive in six-well plates, enabling high-resolution imaging of the living tumor cell distribution following implant and treatment in mice (Figure 3B schematic). Qualitative images of red-fluorescent tumor from representative brain slices show how RHI, LHI, and ICV treatment spatially impact tumor recurrence patterns over time and in anterior/posterior areas of the brain (Figure 3C). Quantitative fluorescence imaging of solid and invasive tumor ($n \geq 12$ slices from two animals per group per time point) was determined by imaging brain slices on an optical imaging system and measuring the flux of photons through regions of interest circumscribing the right hemisphere (containing solid tumor) or left hemisphere (containing invasive tumor). Figure 3D shows that (1) RHI treatment sustainably decreased the primary tumor burden, but not the invasive tumor; (2) LHI treatment decreased the invasive tumor burden near the injection site but not in anterior or posterior regions and had no effect on the solid tumor burden; and (3) ICV treatment sustainably decreased the invasive tumor burden throughout the brain but had a minimal impact on solid tumor growth.

Drug resistance and spatial escape are only two mechanisms for tumor recurrence in advanced GBM. Another potential mechanism limiting treatment durability could be sub-optimal iNSC persistence that results in a lower overall dose of therapeutic protein. A durable

Figure 2. mRNA-seq of solid- and invasive-tumor regions from untreated and recurrent tumors

An overall shift in tumor characteristics after treatment is shown in (A) via PCA and (B) via hierarchical clustering. The plots in (C) display pairwise comparisons of KEGG pathway regulation. Circle size, number of changed genes per pathway; circle position, percentage of changed genes per pathway; circle color, overall significance of pathway changes. Images that include named KEGG pathways in (C) appear in Figure S7.

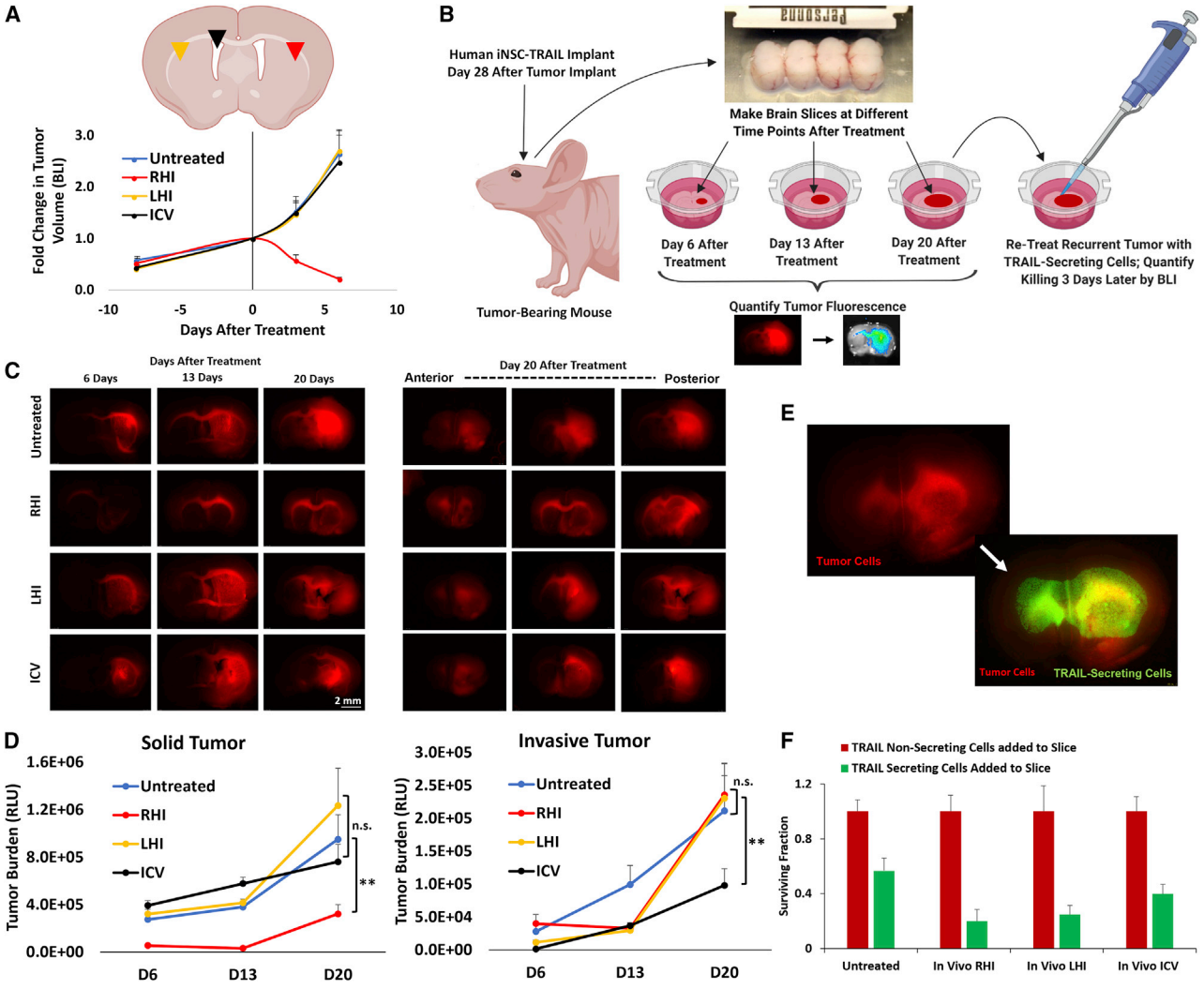

Figure 3. Analyzing spatial tumor recurrence by using living -brain slices

(A) Tumor burden (live-animal BLI) after *in* vivo iNSC-TRAIL treatment via RHI (red), LHI (orange), or ICV (black). (B) Experimental design schematic for (C–F). (C) Left: fluorescence images of tumor burden (red) in representative coronally sectioned brain slices near treatment site generated 6, 13, or 20 days after treatment. Right: fluorescence images of tumor burden in representative anterior and posterior brain slice regions generated 20 days after treatment. (D) Average tumor fluorescence in solid or invasive tumor, calculated from relative light unit (RLU) quantification within ROIs circumscribing right hemisphere (solid tumor) or left hemisphere (invasive tumor); $n \geq 12$. (E) Fluorescence images of a representative brain slice containing red fluorescent tumor (top left) and the same brain slice with added green fluorescent TRAIL-secreting cells (bottom right). (F) Quantification of average surviving-tumor burden- in D20 brain slices 3 days after *ex vivo* re-treatment with TRAIL-secreting cells; $n \geq 6$. Data expressed as mean ± SEM. $^{**}p < 0.01$; $p > 0.05$ = not significant (ns).

cell-based therapy requires that drug carriers survive long term after implantation to sustain drug levels for prolonged tumor suppression. Because we are optimizing our human iNSCs in murine tumor models, expression of MHC antigens on the iNSCs engrafted into the brain can trigger immune-mediated clearance.[28] We previously found that human NSC persistence was reduced to just 20% in 10 days in nude mice with U87 human xenografts.[7] Restoring iNSC drug carrier numbers to model re-dosing—or to model the enhanced persistence that we may observe in future autologous models—could maintain tumoricidal agents at therapeutic doses for lasting tumor suppression, but only if the recurrent tumor retains sensitivity to those agents.

As described above, our mRNA-seq results showed few changes within TRAIL resistance pathways in the recurrent tumor and suggested that these recurrent tumors maintained their sensitivity to TRAIL; however, this method was expensive, cumbersome, and lengthy. Additionally, transcriptomic data are still an indirect result and a step away from functional drug sensitivity data in their ability to predict therapeutic outcomes. Establishing and treating living brain

slices containing naive or recurrent tumor provided a unique platform to rapidly model re-dosing and *functionally* measure any potential losses in drug sensitivity after tumor recurrence. Comparing functional drug sensitivity data from brain slices to our transcriptomic data also served as a test to support or refute tumor-embedded brain slice assays as an effective model for this purpose. Brain slices made from mice 20 days after treatment, when recurrent tumors were largest, were used for this assay. After fluorescence imaging used for Figures 3C and 3D, TRAIL-secreting or control cells were overlaid atop naive and recurrent-tumor-embedded brain slices (Figure 3E). Three days later, bioluminescence of the live tumor cells remaining on the slices was quantified ($n \geq 6$; Figure 3F). The recurrent tumors remained responsive to TRAIL treatment, with reduction in BLI as low as 80%, suggesting that sensitivity to this drug had been retained after tumor recurrence.

Investigating dual-infusion sites and re-dosing strategies to improve iNSC therapy

We next sought to determine whether increasing therapeutic coverage via combined infusion strategies improved durability of iNSC-TRAIL treatment. As our data suggested that ICV treatment effectively killed invasive tumor in both anterior and posterior regions of the brain but was unable to kill the solid tumor, we sought to combine ICV and RHI treatment. We again implanted tumors and allowed 28 days for widespread tumor development before initiating treatment with iNSC-TRAIL at 200,000 cells per region (Figures 4A and 4B). Tumor progression tracked longitudinally via live-animal BLI showed initially effective tumor growth inhibition from both RHI and RHI + ICV (Figure 4C): whereas untreated tumors had grown more than 3-fold just 6 days after treatment initiation, both RHI and RHI + ICV treatment decreased tumor burden by more than 67% ($p < 0.001$). When tumors eventually recurred, there were distinct responders and non-responders in the RHI + ICV group compared with RHI alone. Several mice receiving RHI + ICV treatment lived markedly longer—up to 42 days after treatment—whereas other mice showed minimal increased tumor kill or increased survival from added ICV treatment. This varied efficacy led to an insignificant increase in overall survival between the two treatment groups ($p = 0.17$, RHI [red lines] versus RHI + ICV [purple lines]).

It was unclear what may have caused this varied efficacy, but building off these findings, we next explored the potential of re-dosing to further prolong iNSC treatment durability. Subsets of mice initially receiving RHI + ICV treatment were re-treated in the same manner either 7 or 19 days after initial treatment to explore the impact of re-dosing at (1) the nadir of tumor burden or (2) after tumor recurrence had begun. Longitudinal BLI showed that early re-treatment provided some momentary tumor growth inhibition compared with a single RHI + ICV dose: recurring tumors that had received only a single RHI + ICV dose grew 5.3-fold from day 6 to day 12, whereas tumors receiving re-treatment on day 7 re-grew only 1.9-fold during this time. Similarly, tumors receiving a second dose 19 days after initial treatment re-grew only 2.8-fold over the next 6 days compared with a 5-fold re-growth of tumors receiving only a single dose. Unfortunately, the modest effects of these re-treatments were short-lived and did not lead to any increase in survival over a single RHI + ICV dose (Figure 4B). Interestingly, fluorescence images of coronal brain sections at terminal end points (Figures 4D and S9) revealed that tumors had recurred near iNSC-TRAIL implant sites after RHI + ICV single treatment, whereas early and late re-treatment inhibited tumor recurrence around the original tumor area. Live-animal bioluminescence images supported this finding, revealing that the bulk of tumor recurrence after re-treatment was not occurring around the treatment sites but rather at the most anterior and posterior regions of the brain, away from both the implantation site and regions of CSF flow (Figure 4D, inlaid images, and Figure S10). Unfortunately, despite continually limiting tumor recurrence in the original tumor area, survival was not prolonged compared with single-dose treatment, suggesting that RHI + ICV re-dosing inadequately addressed the invasive tumor.

Notably, in terminal fluorescence images of brains receiving RHI + ICV with late re-dosing, we also detected iNSC-TRAIL cells (Figure S11, green) still residing in the right hemisphere and lateral ventricles and adjacent to areas of lower tumor burden, again suggesting that tumor cells remained sensitive to TRAIL upon re-dosing. We reasoned that the efficacy of re-dosing was reduced because re-infusion in the same location was not adequately addressing novel areas of tumor invasion. This again suggested that treatment failure was less a function of molecular tumor resistance and more dependent on failures in therapeutic coverage. Interestingly, both early and late RHI + ICV re-treatment showed the same variable efficacy as RHI + ICV single treatment: some mice responded no better than mice that received RHI alone, whereas others survived up to 40 days after treatment initiation. Hypotheses regarding the variable efficacy of ICV treatment are discussed below.

To more reproducibly determine the impact of a full iNSC-TRAIL dose delivered at the tumor's invasive front, we directly injected therapeutic iNSCs into the parenchyma of the left hemisphere alongside RHI treatment (RHI + LHI) and monitored tumor bioluminescence (Figures 5A and 5B). Survival analysis showed that RHI + LHI reproducibly and significantly improved overall survival compared with RHI alone ($p < 0.004$; Figure 5C), increasing survival by 25% and permitting mice to survive an average of 34 days post-treatment versus only 27 days compared with RHI alone. Longitudinal BLI imaging curves of average RHI and RHI + LHI growth (Figure 5A) showed a similar recurrence pattern due to one fast-growing tumor in the RHI + LHI group (Figure 5B).

The benefits of RHI + LHI treatment were even more evident in correlative *ex vivo* brain slice analysis (Figures 5D and 5E). High-resolution imaging of the living slices taken from treated mice with recurrent tumors revealed that RHI + LHI decreased solid-tumor burden more fully and durably than RHI alone ($p < 0.0001$ on day 6; $p < 0.0001$ on day 20) and decreased invasive-tumor burden more fully and durably than LHI alone ($p < 0.01$ on day 6; $p < 1e–5$ on day 20). Together, these data begin to describe the ways in which

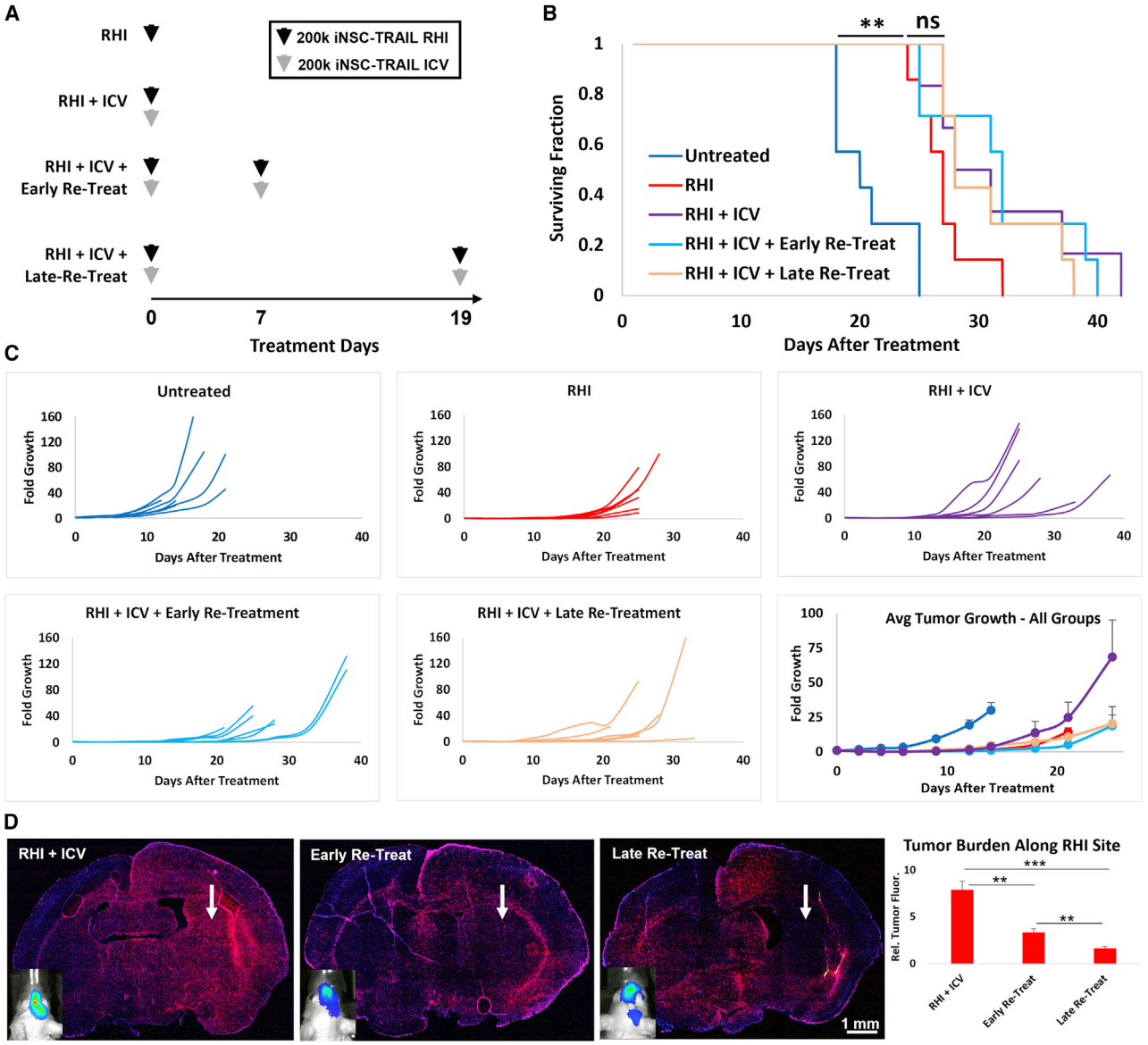

Figure 4. *In vivo* survival study

(A) Schematic showing treatment and re-treatment schedule. (B) Kaplan-Meier curve displaying survival of mice in each group. (C) Growth curves of tumors in individual mice within each group (BLI). Each line stops at the time point at which mouse body condition score necessitated euthanasia. Bottom right: average tumor growth curve for all groups; n = 6–7 mice per group. (D) Fluorescence images of cryo-sectioned coronal brain sections (10 μm thickness). Inlaid live-mouse BLI of *in vivo* tumor burden (additional images in Figure S10) correlates with fluorescence images in (D) and Figure 3, showing ability of re-treatment to kill tumor near the RHI implant/re-treatment site but not in anterior or posterior regions. Tumor burden along the RHI site (white arrows) was measured via background-subtracted fluorescence quantification in fluorescence cryosections (n = 4 representative areas of 1 mm^2 each; also shown in Figure S9). Data expressed as mean ± SEM. **$p < 0.01$; $p > 0.05$ = not significant (ns).

infusing iNSCs into more than one location increases therapeutic coverage, addresses the spatial evasion of tumor cells that allows them to escape therapy, and improves the durable suppression of invasive late-stage GBM by therapeutic iNSCs.

The schematic in Figure 6 qualitatively summarizes our *in vivo* and *ex vivo* findings across all eight treatment regimens in this study, comparing the ability of each with control tumor growth in various regions of the brain. Although all tumors eventually recurred after treatment ended, comparing tumor burden 20 days after treatment revealed significant differences in efficacy. Mice receiving RHI + LHI treatment showed the greatest and most durable efficacy throughout the brain, acquired the largest survival benefit, and were the only group to survive significantly longer than mice receiving RHI treatment alone.

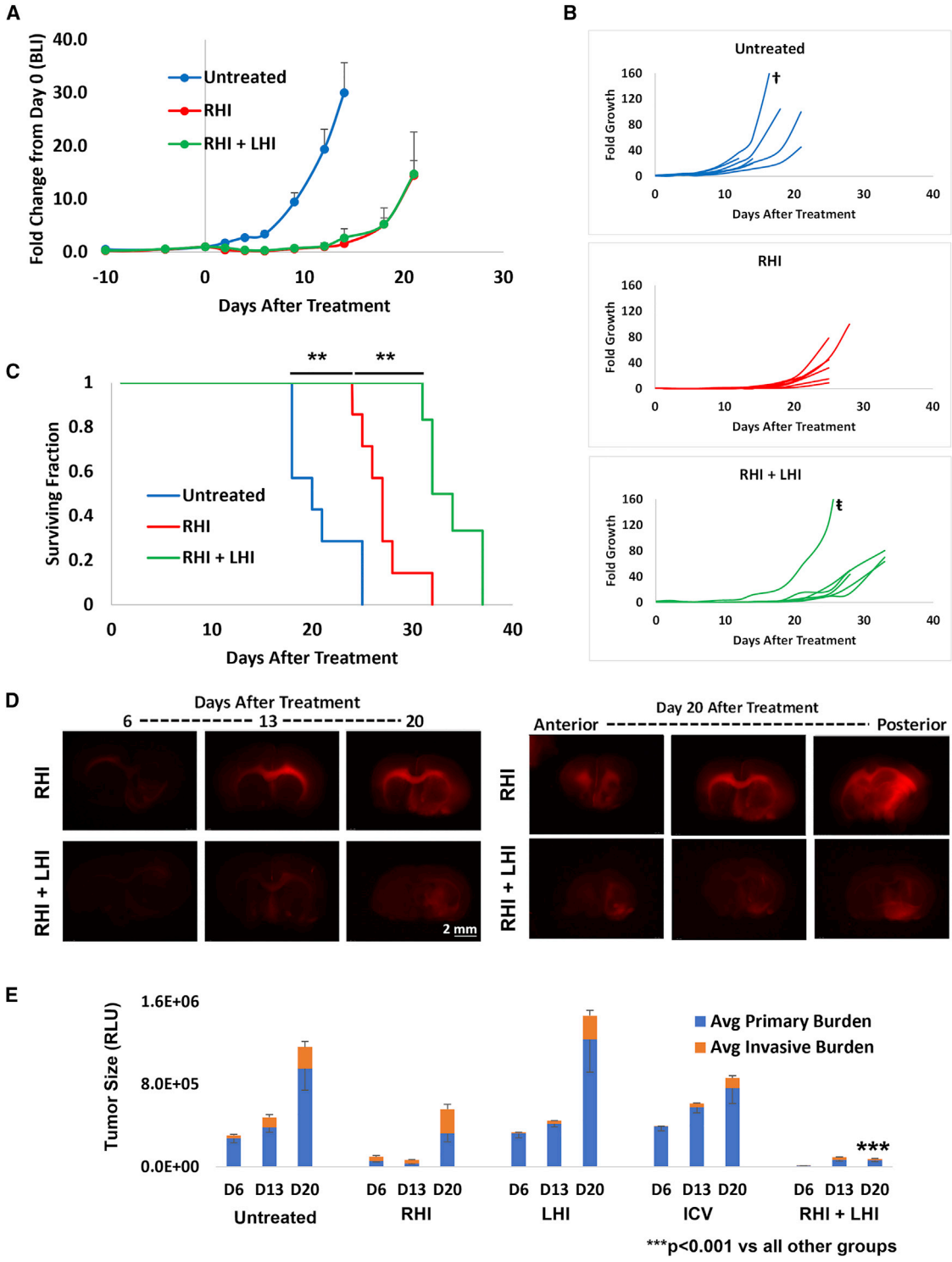

Figure 5. Testing RHI + LHI treatment

(A) Average tumor burden after RHI or RHI + LHI treatment as quantified by BLI; n = 6–7. (B) Growth curves of tumors in individual mice within each group. †Last recorded tumor burden (untreated group), 1,130-fold growth 25 days after treatment initiation. ‡Last recorded tumor burden (RHI + LHI group), 370-fold growth 28 days after treatment

(legend continued on next page)

DISCUSSION

Advancing iNSC therapy depends on our increased understanding of how and from where the tumor recurs. By creatively treating an aggressive model of late-stage GBM, we have thus developed unique methods to interrogate how spatial escape and acquired drug resistance may influence therapeutic efficacy. Analyzing re-growth patterns of advanced GBM by measuring tumor burden in living brain slices has given us deeper insight into how these tumors respond to treatment. Maintaining and re-treating the brain slices has also allowed us to re-challenge the recurrent tumors with TRAIL *ex vivo* and rapidly quantify a functional tumor response to correlate with our transcriptomic data. By combining the transcriptomic, *ex vivo*, and *in vivo* data reported here, we can begin to understand not only the story of this specific model but also broader themes that will influence overall treatment strategies:

This tumor model possessed significant TRAIL sensitivity, leading to effective tumor kill near the iNSC-TRAIL implantation sites after implantation of only 200,000 cells via RHI. Although this implantation route was able to kill a majority of the local solid tumor, it was not enough to induce killing of invasive tumor cells in the contralateral hemisphere. Even so, our transcriptomic data revealed significant changes in the invasive tumor after RHI treatment, suggesting that some sub-therapeutic dose did indeed reach these cells. Interestingly, these cells that treatment changed but did not kill look transcriptomically similar to the solid recurrent tumor after RHI treatment, suggesting that the eradicated solid tumor region was re-populated by tumor cells that had evaded treatment via spatial escape and thus received only a sub-therapeutic dose. Furthermore, these recurrent cells maintained their sensitivity to TRAIL, confirmed by mRNA-seq, *ex vivo* functional analysis on brain slices, and *in vivo* testing. These data suggest that (1) iNSC-TRAIL cells implanted in the right hemisphere of the brain can provide some sub-therapeutic dose into the contralateral hemisphere via a combination of iNSC-TRAIL migration and diffusion of secreted TRAIL; (2) distant tumor cells that survive treatment are no longer treatment naive, even as they maintain sensitivity to TRAIL; and (3) overlapping multiple areas of sub-therapeutic doses may provide combined doses adequate to kill tumor cells.

We attempted to increase therapeutic coverage of iNSC-TRAIL and overlap areas of sub-therapeutic dose by implanting iNSC-TRAIL into the brain's ventricular system, and although RHI + ICV treatment improved survival for some mice, overall impact was not statistically significant compared with solid treatment only. Our data indicating that the recurrent tumor was still sensitive to TRAIL suggested that we also attempt to increase survival by re-dosing RHI + ICV either 7 or 19 days after initial treatment. We found that re-treatment did not increase survival, even though a second dose of iNSC-TRAIL into both regions still successfully killed tumor cells near the RHI implant sites. In this case, the tumor cells that had escaped initial treatment had continued to invade, spreading to the most anterior and posterior regions of the brain and farther from ventricular flow.

For ICV therapy to provide maximal therapeutic coverage, iNSC-TRAIL cells must homogeneously circulate through the ventricular system, but it is known that mass effects from growing GBM can significantly displace and constrict the brain's ventricular system.[29] We speculate that the inconsistent results obtained from using ICV therapy in these mice may be due to mouse-to-mouse variability in ventricular displacement. Our group has previously modeled ICV injection of therapeutic cells,[30,31] but not in a model of large, late-stage brain cancer. Further use of ICV infusion against this tumor model may require correlative imaging techniques as seen in the clinic.

Increased tumor kill and survival via dose overlap was most consistent in RHI + LHI treatment. RHI alone provided only a sub-therapeutic dose to the invasive tumor and failed to kill those cells, while LHI alone failed to kill the solid tumor. In contrast, RHI + LHI decreased the solid tumor burden more fully and durably than RHI alone and decreased the invasive tumor burden more fully and durably than LHI alone. This additive effect from overlapping dose regions suggests that rationally designed spacing of treatment nodes may accumulate higher doses both close to an iNSC implant site as well as within regions of dose overlap.

iNSC-TRAIL is especially equipped to maximize both dose overlap and overall therapeutic coverage as the cells actively migrate toward the tumor after implant while TRAIL is secreted and diffuses throughout the brain.[16] Off-target toxicity is minimal because TRAIL must bind to death receptors upregulated in tumor cells. We have previously compared iNSC-TRAIL with iNSC-TK, which express the enzyme thymidine kinase to help catalyze exogenously added ganciclovir (GCV) to the DNA intercalator GCV triphosphate, a drug with more widespread toxicity.[18] Although TK/GCV therapy does not have as many issues with drug resistance compared with TRAIL, iNSC-TK cells must directly interact with tumor cells to initiate the therapeutic effect, decreasing therapeutic coverage. Likewise, embryonic stem cells have been shown to mediate tumor kill via Fas/FasL but also require cell-cell interaction.[32]

These studies provide immense insight into the spatial, functional, and transcriptomic evolution of an aggressive late-stage brain tumor. The pervasive growth and invasion of tumor cells in this model allowed us to robustly test iNSC-TRAIL therapy and arrive at

initiation. (C) Kaplan-Meier survival plot; n = 6–7. (D) Qualitative fluorescence images of coronally sliced tumor-bearing brains comparing tumor burden in mice after RHI or RHI + LHI treatment at 6, 13, and 20 days after treatment (left) or in regions anterior and posterior to the iNSC-TRAIL implantation sites (RHI + LHI data combined with RHI data presented in Figure 3C). (E) Quantification of average recurrent solid and invasive tumor, comparing Untreated, RHI, LHI, ICV, and RHI + LHI groups (combined with data presented in Figure 3C); $n \geq 12$. Data expressed as mean ± SEM. $^{**}p < 0.01$; $^{***}p < 0.001$.

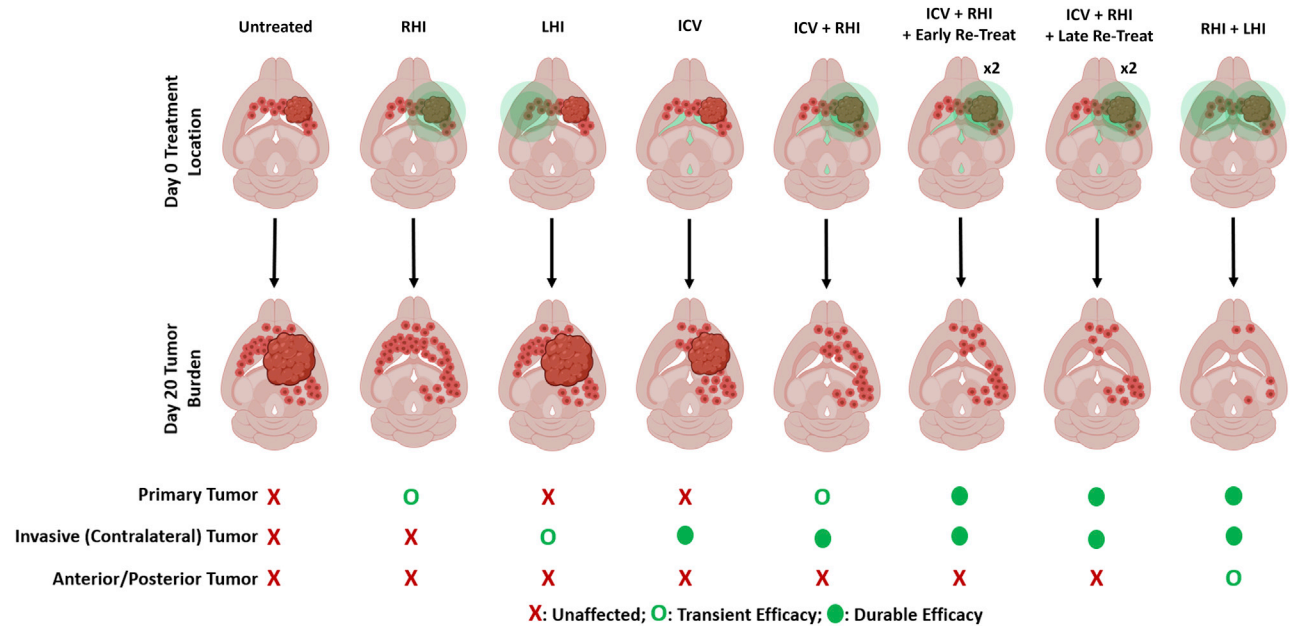

Figure 6. Summary of treatment efficacies

This schematic qualitatively summarizes the relative efficacy and durability of tumor growth inhibition among all treatment groups. Our cumulative data suggest that, given an initially large solid tumor mass with significant invasion into the contralateral hemisphere (day 0 treatment location, red), the placement of each treatment (day 20 treatment location, green) resulted in different tumor recurrence patterns (day 20 tumor burden, red). Relative tumor killing of each treatment was qualitatively ranked as "Unaffected," "Transient Efficacy," or "Durable Efficacy."

conclusions that would have been inaccessible using other models. We were able to combine the fidelity of mRNA-seq and *in vivo* studies with the speed and spatial resolution of living brain slice technology, allowing us to observe and quantitatively assay resistance/recurrence mechanisms of these tumors in response to iNSC-TRAIL therapy. Our core conclusions are thus: (1) modeling tumor recurrence using living *ex vivo* brain slice models allows comprehensive quantification of regrowth patterns and rapid, functional analysis of drug-induced killing; (2) tumor resistance and recurrence can occur not only from decreased drug sensitivity but also by spatial changes in regrowth; and (3) overlapping multiple areas of sub-therapeutic doses may provide doses adequate to kill tumor cells. Our laboratory continues to make improvements in iNSC persistence, migration, and drug output, and future studies will continue to optimize repeated and multi-site dosing regimens to achieve both high drug concentration and high spatial coverage to combat tumor recurrence, cognizant that dose patterns may need to be modified as the tumor re-grows. These findings provide important guidance toward optimizing iNSC therapy as we advance toward the ultimate goal of improving GBM patient care in the clinical setting.

MATERIALS AND METHODS

Animal ethics statement

All work performed on female athymic nude mice (therapy studies) or Sprague-Dawley rats (brain slice preparation) was approved by the Institutional Animal Care and Use Committee at the University of North Carolina-Chapel Hill or Duke University.

Cell lines

G-EF and G-FBS cells were gifts from H. Wakimoto (Massachusetts General Hospital). Human fibroblasts were provided by W. Kauffman (University of North Carolina [UNC] School of Medicine). All cells were grown *in vitro* as previously described.[6,15] G-FBS cells were grown in DMEM (Gibco) + 10% FBS and 1% penicillin-streptomycin; G-EF cells were grown in Neurobasal medium (Gibco) with 7.5 mL L-glutamine, 10 mL B27 supplement, 2.5 mL N2 supplement, 1 mg heparin, 10 μg EGF, 10 μg FGF, and 2.5 mL anti-anti. Lentiviral vectors (LVs) encoding hTERT and SOX2 were purchased from Addgene. All complementary DNAs (cDNAs) were under the control of the tetracycline promoter.

Lentiviral vectors

In addition to the re-programming vectors, the following LVs were used in this study: eGFP fused to firefly luciferase (LV-eGFP-FL), mCherry protein fused to firefly luciferase (LV-mC-FL), and a secreted variant of TRAIL co-expressed with eGFP (LV-sTR-eGFP). LV construction and cellular transduction have been described previously.[6]

iNSC generation

iNSC generation was carried out as previously described.[16–18,31] Human fibroblasts were transduced using a LV cocktail containing TRAIL, hTERT, and SOX2 in a medium containing protamine sulfate (5 mg/mL, Sigma). Transfected human fibroblasts were puromycin selectable to ensure maximal iNSC population at each induction of

transdifferentiation. To induce transdifferentiation, the medium was changed to STEMdiff Neural Induction Medium (StemCell Technologies) containing doxycycline (10 μg/mL, Sigma). Medium was changed every third day for 6 days.

In vivo tumor studies

Patient-matched established tumor

Previously, GBM biopsy material from a single patient had been separated and cultured in different media that selected for two distinct cell types and separately characterized *in vivo*.[33–36] We obtained limited-passage solid cells that had been selected either in stem cell medium containing EGF and FGF (G-EF cells, p28) or in DMEM with FBS (G-FBS cells, p18) as a gift from the Wakimoto laboratory (Massachusetts General Hospital, Boston, MA). G-EF cells were infected with mCh-Fluc, and G-FBS cells were infected with GFP-FLuc via lentiviral infection in our laboratory. Cells were implanted *in vivo* at a rate of 1 μL/min at coordinates (ML, AP, DV = 2.7, 0, 3.5) from bregma at a ratio of G-EF/G-FBS of 1:5 (600,000 cells/mouse). Tumors were allowed to grow for 28 days before therapeutic iNSCs were implanted into the established tumor.

In the initial study to determine growth kinetics, tumors were implanted into 40 mice (ML, AP, DV = 2.7, 0, 3.5), and 28 days later, mice were stratified and grouped by tumor volume (BLI), and 200,000 iNSC-TRAIL cells were either implanted into the hemisphere containing the solid tumor (ML, AP, DV = 2.7, 0, 3.5; n = 8), the contralateral hemisphere (ML, AP, DV = −2.7, 0, 3.5; n = 8), or 400,000 iNSC-TRAIL cells were implanted into the left lateral ventricle (ML, AP, DV = −1.1, 0, 2.5; n = 7), and n = 8 mice were left untreated. Cells were implanted at a rate of 1 μL/min.

In the survival studies, tumors were implanted into 40 mice (ML, AP, DV = 2.7, 0, 3.5), and 28 days later, mice were stratified and grouped by tumor volume (BLI), and 200,000 iNSC-TRAIL cells per location were implanted into (1) the hemisphere containing the solid tumor (n = 7), (2) the solid hemisphere and the contralateral hemisphere (n = 6), or (3) the solid hemisphere and the left lateral ventricle (Solid + ICV, n = 20). Seven mice were left untreated. At t = 7 days after initial treatment, mice initially receiving Solid + ICV treatment (n = 20) were re-stratified and grouped by tumor volume and seven mice received a second Solid + ICV treatment (early re-treatment). At t = 19 days after initial treatment, remaining mice that had received only one Solid + ICV treatment (now n = 13) were re-stratified and grouped by tumor volume, and seven mice received a second Solid + ICV treatment (late re-treatment).

Live-animal bioluminescence imaging

An IVIS Kinetic (PerkinElmer) imaging system was used for all *in vivo* bioluminescence imaging. Mice were imaged approximately every 3 days. XenoLight D-Luciferin (PerkinElmer) was injected intraperitoneally (i.p.) into tumor-bearing mice at a dose of 3 mg/mouse in 200 μL of PBS. Mice were imaged after an incubation time of 10 min, and bioluminescence within a standard region of interest (ROI) was quantified in total flux of photons per second. All ROIs were of equal size and shape.

Preparation of brains at study end point

At study end points, mice were anesthetized with isofluorane, and a cardiac perfusion technique was used to perfuse blood vessels with 5 mL of PBS followed by 5 mL of 10% neutral-buffered formalin. Brains were dissected and soaked in 10% formalin overnight. Fluorescence imaging was then used to cut the brain coronally across the region of tumor implant. Both halves were moved to a 30% sucrose solution in PBS overnight before being embedded in OCT solution for frozen sectioning via cryostat.

Fluorescence imaging

Tumor-bearing brains in OCT were sectioned on a cryostat at a thickness of 6 μm. OCT was dissolved in PBS for 20 min, and Hoechst nuclear stain was applied. Sections were washed, and coverslips were mounted using Prolong Gold mounting medium. Tumor fluorescence was imaged using an EVOS FL Auto system with DAPI, GFP, and Texas Red filters.

Brain slice studies

Mice were used from each treatment group in the initial study to measure tumor growth kinetics. At 6, 13, and 20 days after treatment, live brains were dissected from two representative tumor-bearing mice from each group. Brains were mounted and sectioned on a vibratome (Leica VT1000 S) at a thickness of 350 μm. The slices were cut while immersed in ice-cold artificial cerebrospinal fluid and then transferred to multi-well plates on the top surface of semi-solidified culture medium (Neurobasal A medium supplemented with 15% heat-inactivated horse serum, 10 mM KCl, 10 mM HEPES, 100 U/mL penicillin-streptomycin, 1 mM sodium pyruvate, 1 mM L-glutamine, and 0.5% reagent-grade agarose.) The slices were immediately imaged qualitatively on a Leica surgical microscope using LAS-X software and then imaged on an AMI optical imaging system (Spectral Instruments Imaging) for quantitative fluorescence imaging. Tumors in brain slices harvested 20 days after treatment were re-treated *ex vivo*. Approximately 20,000 iNSC-TRAIL or iNSC-GFP cells in 5 μL of PBS were added atop each slice. Slices were then incubated under 5% CO_2 at 32°C for 3 days, at which point bioluminescence of surviving tumor cells was quantified. Luciferin (1.5 mg) in 1 mL of PBS was added to each well, covering the brain slices. Three minutes after addition, the bioluminescence of each slice was measured.

RNA-seq studies

At the time of tumor progression requiring euthanasia, three randomly selected untreated and solid-treated brains from our survival study were fixed via cardiac perfusion with PBS and 4% paraformaldehyde (PFA), followed by overnight incubations in 4% PFA and a 30% sucrose solution in PBS. Brains were cut coronally along the implantation site, frozen in OCT, sectioned on a cryostat at a thickness of 60 μm, and added to glass slices. Using a fluorescence-guided surgical microscope, distinct fluorescent regions of solid and invasive tumor were carefully excised with fine surgical tweezers. For each

brain, tumor regions were collected from four consecutive sections and pooled into two tubes: one tube for solid-tumor regions and one for invasive-tumor regions, containing buffer to begin cell lysis for RNA extraction (Melting Buffer + Proteinase K, Invitrogen PureLink FFPE Total RNA Isolation Kit). The kit's protocol was followed to retrieve purified RNA samples. The Advanced Analytics Core at UNC measured RNA integrity number (RIN) values for each sample and conducted whole-transcriptome mRNA-seq using an Illumina system.

To analyze, we classified transcripts as originating from human tissue by using Xenome with default parameters and subsequently used Salmon 1.3.0 for alignment and transcript quantification using default parameters and the GC bias correction. We then performed differential expression analysis using DESeq2 3.12, keeping only genes wherein at least three samples had a count of 10 or higher. Generalized PCA was calculated using the glmpca R package.

The reference to the tools in order are:

Xenome: https://academic.oup.com/bioinformatics/article/28/12/i172/269972 [academic.oup.com].

Salmon: https://www.ncbi.nlm.nih.gov/pmc/articles/PMC5600148/ [ncbi.nlm.nih.gov].

DESeq2: https://genomebiology.biomedcentral.com/articles/10.1186/s13059-014-0550-8 [genomebiology.biomedcentral.com].

Statistical analysis

RNA-seq studies were analyzed as described above. Other data were analyzed by Student's t test when two groups were compared, by one-way ANOVA with Bonferroni post hoc analysis when more than two groups were compared, or by the log rank test when survival times of mice were compared in Kaplan-Meier curves. Data are expressed as mean ± SEM, and significance between groups is denoted by $^{*}p < 0.05$, $^{**}p < 0.01$, and $^{***}p < 0.001$; $p > 0.05$ is considered not significant.

DATA AND MATERIALS AVAILABILITY

All data, code, and materials used in this analysis can be made available in some form to any researcher for purposes of reproducing or extending the analyses.

SUPPLEMENTAL INFORMATION

Supplemental information can be found online at https://doi.org/10.1016/j.omto.2022.06.004.

ACKNOWLEDGMENTS

This work was supported by National Institutes of Health Grant NIHR01NS099368, by the National Center for Advancing Translational Sciences Grant U01TR003715, by the Eshelman Institute for Innovation, and by Accelerate Brain Cancer Cure. A.B.S. was supported by a TL1 fellowship from the National Center for Advancing Translational Sciences, NIH Grant TL1TR002491. We would like to thank the laboratory of Hiroaki Wakimoto for gifting us their G-EF and G-FBS cell lines. We would also like to thank the Advanced Analytics Core at UNC for guiding and running our sequencing experiments. Figures contain images created with BioRender.com.

AUTHOR CONTRIBUTIONS

Study design: A.B.S. and S.H.; *in vivo* studies: A.B.S. and A.V.; *ex vivo* preparation: D.D. and A.B.S.; sequencing analysis: D.M., A.B., and T.G.; securing funding: S.H. and S.F.

DECLARATION OF INTERESTS

Shawn Hingtgen is the founder of Falcon Therapeutics.

REFERENCES

1. Adamson, C., Kanu, O.O., Mehta, A.I., Di, C., Lin, N., Mattox, A.K., and Bigner, D.D. (2009). Glioblastoma multiforme: a review of where we have been and where we are going. Expert Opin. Investig. Drugs *18*, 1061–1083. https://doi.org/10.1517/13543780903052764.

2. Erpolat, O.P., Akmansu, M., Goksel, F., Bora, H., Yaman, E., and Büyükberber, S. (2009). Outcome of newly diagnosed glioblastoma patients treated by radiotherapy plus concomitant and adjuvant temozolomide: a long-term analysis. Tumori *95*, 191–197. https://doi.org/10.1177/030089160909500210.

3. Stupp, R., Hegi, M.E., Mason, W.P., van den Bent, M.J., Taphoorn, M.J., Janzer, R.C., Ludwin, S.K., Allgeier, A., Fisher, B., Belanger, K., et al. (2009). Effects of radiotherapy with concomitant and adjuvant temozolomide versus radiotherapy alone on survival in glioblastoma in a randomised phase III study: 5-year analysis of the EORTC-NCIC trial. Lancet Oncol. *10*, 459–466. https://doi.org/10.1016/S1470-2045(09)70025-7.

4. Aboody, K.S., Brown, A., Rainov, N.G., Bower, K.A., Liu, S., Yang, W., Small, J.E., Herrlinger, U., Ourednik, V., Black, P.M., et al. (2000). Neural stem cells display extensive tropism for pathology in adult brain: evidence from intracranial gliomas. Proc. Natl. Acad. Sci. U S A *97*, 12846–12851. https://doi.org/10.1073/pnas.97.23.12846.

5. Ahmed, A.U., Alexiades, N.G., and Lesniak, M.S. (2010). The use of neural stem cells in cancer gene therapy: predicting the path to the clinic. Curr. Opin. Mol. Ther. *12*, 546–552.

6. Hingtgen, S.D., Kasmieh, R., van de Water, J., Weissleder, R., and Shah, K. (2010). A novel molecule integrating therapeutic and diagnostic activities reveals multiple aspects of stem cell-based therapy. Stem Cells *28*, 832–841. https://doi.org/10.1002/stem.313.

7. Shah, K., Hingtgen, S., Kasmieh, R., Figueiredo, J.L., Garcia-Garcia, E., Martinez-Serrano, A., Breakefield, X., and Weissleder, R. (2008). Bimodal viral vectors and in vivo imaging reveal the fate of human neural stem cells in experimental glioma model. J. Neurosci. *28*, 4406–4413. https://doi.org/10.1523/jneurosci.0296-08.2008.

8. Aboody, K.S., Najbauer, J., and Danks, M.K. (2008). Stem and progenitor cell-mediated tumor selective gene therapy. Gene Ther. *15*, 739–752. https://doi.org/10.1038/gt.2008.41.

9. Aboody, K.S., Najbauer, J., Metz, M.Z., D'Apuzzo, M., Gutova, M., Annala, A.J., Synold, T.W., Couture, L.A., Blanchard, S., Moats, R.A., et al. (2013). Neural stem cell-mediated enzyme/prodrug therapy for glioma: preclinical studies. Sci. Transl. Med. *5*, 184ra59. https://doi.org/10.1126/scitranslmed.3005365.

10. Hingtgen, S., Kasmieh, R., Elbayly, E., Nesterenko, I., Figueiredo, J.L., Dash, R., Sarkar, D., Hall, D., Kozakov, D., Vajda, S., et al. (2012). A first-generation multifunctional cytokine for simultaneous optical tracking and tumor therapy. PLoS One *7*, e40234. https://doi.org/10.1371/journal.pone.0040234.

11. Hingtgen, S., Ren, X., Terwilliger, E., Classon, M., Weissleder, R., and Shah, K. (2008). Targeting multiple pathways in gliomas with stem cell and viral delivered S-TRAIL and Temozolomide. Mol. Cancer Ther. *7*, 3575–3585. https://doi.org/10.1158/1535-7163.MCT-08-0640.

12. Sasportas, L.S., Kasmieh, R., Wakimoto, H., Hingtgen, S., van de Water, J.A.J.M., Mohapatra, G., Figueiredo, J.L., Martuza, R.L., Weissleder, R., and Shah, K. (2009).

Assessment of therapeutic efficacy and fate of engineered human mesenchymal stem cells for cancer therapy. Proc. Natl. Acad. Sci. U S A *106*, 4822–4827. https://doi.org/10.1073/pnas.0806647106.

13. Ehtesham, M., Kabos, P., Kabosova, A., Neuman, T., Black, K.L., and Yu, J.S. (2002). The use of interleukin 12-secreting neural stem cells for the treatment of intracranial glioma. Cancer Res. *62*, 5657–5663.

14. Tobias, A.L., Thaci, B., Auffinger, B., Rincón, E., Balyasnikova, I.V., Kim, C.K., Han, Y., Zhang, L., Aboody, K.S., Ahmed, A.U., and Lesniak, M.S. (2013). The timing of neural stem cell-based virotherapy is critical for optimal therapeutic efficacy when applied with radiation and chemotherapy for the treatment of glioblastoma. Stem Cell Transl. Med. *2*, 655–666. https://doi.org/10.5966/sctm.2013-0039.

15. Bagó, J.R., Alfonso-Pecchio, A., Okolie, O., Dumitru, R., Rinkenbaugh, A., Baldwin, A.S., Miller, C.R., Magness, S.T., and Hingtgen, S.D. (2016). Therapeutically engineered induced neural stem cells are tumour-homing and inhibit progression of glioblastoma. Nat. Commun. *7*, 10593. https://doi.org/10.1038/ncomms10593.

16. Bagó, J.R., Okolie, O., Dumitru, R., Ewend, M.G., Parker, J.S., Werff, R.V., Underhill, T.M., Schmid, R.S., Miller, C.R., and Hingtgen, S.D. (2017). Tumor-homing cytotoxic human induced neural stem cells for cancer therapy. Sci. Transl. Med. *9*, eaah6510. https://doi.org/10.1126/scitranslmed.aah6510.

17. Buckley, A., Hagler, S.B., Lettry, V., Bagó, J.R., Maingi, S.M., Khagi, S., Ewend, M.G., Miller, C.R., and Hingtgen, S.D. (2020). Generation and profiling of tumor-homing induced neural stem cells from the skin of cancer patients. Mol. Ther. *28*, 1614–1627. https://doi.org/10.1016/j.ymthe.2020.04.022.

18. Satterlee, A.B., Dunn, D.E., Lo, D.C., Khagi, S., and Hingtgen, S. (2019). Tumoricidal stem cell therapy enables killing in novel hybrid models of heterogeneous glioblastoma. Neuro Oncol. *21*, 1552–1564. https://doi.org/10.1093/neuonc/noz138.

19. Vollmann-Zwerenz, A., Leidgens, V., Feliciello, G., Klein, C.A., and Hau, P. (2020). Tumor cell invasion in glioblastoma. Int. J. Mol. Sci. *21*, 1932. https://doi.org/10.3390/ijms21061932.

20. Maklad, A., Sharma, A., and Azimi, I. (2019). Calcium signaling in brain cancers: roles and therapeutic targeting. Cancers *11*, 145. https://doi.org/10.3390/cancers11020145.

21. Leclerc, C., Haeich, J., Aulestia, F.J., Kilhoffer, M.C., Miller, A.L., Néant, I., Webb, S.E., Schaeffer, E., Junier, M.P., Chneiweiss, H., and Moreau, M. (2016). Calcium signaling orchestrates glioblastoma development: facts and conjunctures. Biochim. Biophys. Acta *1863*, 1447–1459. https://doi.org/10.1016/j.bbamcr.2016.01.018.

22. Zheng, L., Zhou, Z.R., Yu, Q., Shi, M., Yang, Y., Zhou, X., Li, C., and Wei, Q. (2020). The definition and delineation of the target area of radiotherapy based on the recurrence pattern of glioblastoma after temozolomide chemoradiotherapy. Front. Oncol. *10*, 615368. https://doi.org/10.3389/fonc.2020.615368.

23. Misra, A., Ganesh, S., Shahiwala, A., and Shah, S.P. (2003). Drug delivery to the central nervous system: a review. J. Pharm. Pharm. Sci. *6*, 252–273.

24. Fleischhack, G., Jaehde, U., and Bode, U. (2005). Pharmacokinetics following intraventricular administration of chemotherapy in patients with neoplastic meningitis. Clin. Pharmacokinet. *44*, 1–31. https://doi.org/10.2165/00003088-200544010-00001.

25. Hashemi-Sadraei, N., and Peereboom, D.M. (2010). Review: chemotherapy in newly diagnosed primary central nervous system lymphoma. Ther. Adv. Med. Oncol. *2*, 273–292. https://doi.org/10.1177/1758834010365330.

26. Imataka, G., Nakagawa, E., Yamanouchi, H., and Arisaka, O. (2011). Drug-indiced aseptic meningitis: development of subacute sclerosing panencephalitis following repeated intraventricular infusion therapy with interferon alpha/beta. Cell Biochem. Biophys. *61*, 699–701. https://doi.org/10.1007/s12013-011-9228-y.

27. Tsuboi, Y., Doh-Ura, K., and Yamada, T. (2009). Continuous intraventricular infusion of pentosan polysulfate: clinical trial against prion diseases. Neuropathology *29*, 632–636. https://doi.org/10.1111/j.1440-1789.2009.01058.x.

28. Weinger, J.G., Weist, B.M., Plaisted, W.C., Klaus, S.M., Walsh, C.M., and Lane, T.E. (2012). MHC mismatch results in neural progenitor cell rejection following spinal cord transplantation in a model of viral-induced demyelination. Stem Cells *30*, 2584–2595. https://doi.org/10.1002/stem.1234.

29. Steed, T.C., Treiber, J.M., Brandel, M.G., Patel, K.S., Dale, A.M., Carter, B.S., and Chen, C.C. (2018). Quantification of glioblastoma mass effect by lateral ventricle displacement. Sci. Rep. *8*, 2827. https://doi.org/10.1038/s41598-018-21147-w.

30. Jiang, W., Yang, Y., Mercer-Smith, A.R., Valdivia, A., Bago, J.R., Woodell, A.S., Buckley, A.A., Marand, M.H., Qian, L., Anders, C.K., and Hingtgen, S.D. (2021). Development of next-generation tumor-homing induced neural stem cells to enhance treatment of metastatic cancers. Sci. Adv. *7*, eabf1526. https://doi.org/10.1126/sciadv.abf1526.

31. Bomba, H.N., Sheets, K.T., Valdivia, A., Khagi, S., Ruterbories, L., Mariani, C.L., Borst, L.B., Tokarz, D.A., and Hingtgen, S.D. (2021). Personalized-induced neural stem cell therapy: generation, transplant, and safety in a large animal model. Bioeng. Transl. Med. *6*, e10171. https://doi.org/10.1002/btm2.10171.

32. Li, Y., Fan, Y., Xu, J., Zhang, P., Jiang, T., Dai, M., and Li, L. (2018). Genome-wide RNA-Seq identifies Fas/FasL-mediated tumoricidal activity of embryonic stem cells. Int. J. Cancer *142*, 1829–1841. https://doi.org/10.1002/ijc.31201.

33. Wakimoto, H., Kesari, S., Farrell, C.J., Curry, W.T., Jr., Zaupa, C., Aghi, M., Kuroda, T., Stemmer-Rachamimov, A., Shah, K., Liu, T.C., et al. (2009). Human glioblastoma-derived cancer stem cells: establishment of invasive glioma models and treatment with oncolytic herpes simplex virus vectors. Cancer Res. *69*, 3472–3481. https://doi.org/10.1158/0008-5472.CAN-08-3886.

34. Rheinbay, E., Suvà, M., Gillespie, S.M., Wakimoto, H., Patel, A.P., Shahid, M., Oksuz, O., Rabkin, S.D., Martuza, R.L., Rivera, M.N., et al. (2013). An aberrant transcription factor network essential for Wnt signaling and stem cell maintenance in glioblastoma. Cell Rep. *3*, 1567–1579. https://doi.org/10.1016/j.celrep.2013.04.021.

35. Suvà, M., Rheinbay, E., Gillespie, S.M., Patel, A.P., Wakimoto, H., Rabkin, S.D., Riggi, N., Chi, A.S., Cahill, D.P., Nahed, B.V., et al. (2014). Reconstructing and reprogramming the tumor-propagating potential of glioblastoma stem-like cells. Cell *157*, 580–594. https://doi.org/10.1016/j.cell.2014.02.030.

36. Wakimoto, H., Mohapatra, G., Kanai, R., Curry, W.T., Jr., Yip, S., Nitta, M., Patel, A.P., Barnard, Z.R., Stemmer-Rachamimov, A.O., Louis, D.N., et al. (2012). Maintenance of primary tumor phenotype and genotype in glioblastoma stem cells. Neuro Oncol. *14*, 132–144. https://doi.org/10.1093/neuonc/nor195.

OMTO, Volume *26*

Supplemental information

Spatiotemporal analysis of induced neural stem cell therapy to overcome advanced glioblastoma recurrence

Andrew B. Satterlee, Denise E. Dunn, Alain Valdivia, Daniel Malawsky, Andrew Buckley, Timothy Gershon, Scott Floyd, and Shawn Hingtgen

<u>Supplementary Material:</u> Spatiotemporal Analysis of Induced Neural Stem Cell Therapy to Overcome Advanced Glioblastoma Recurrence

Figure S1:

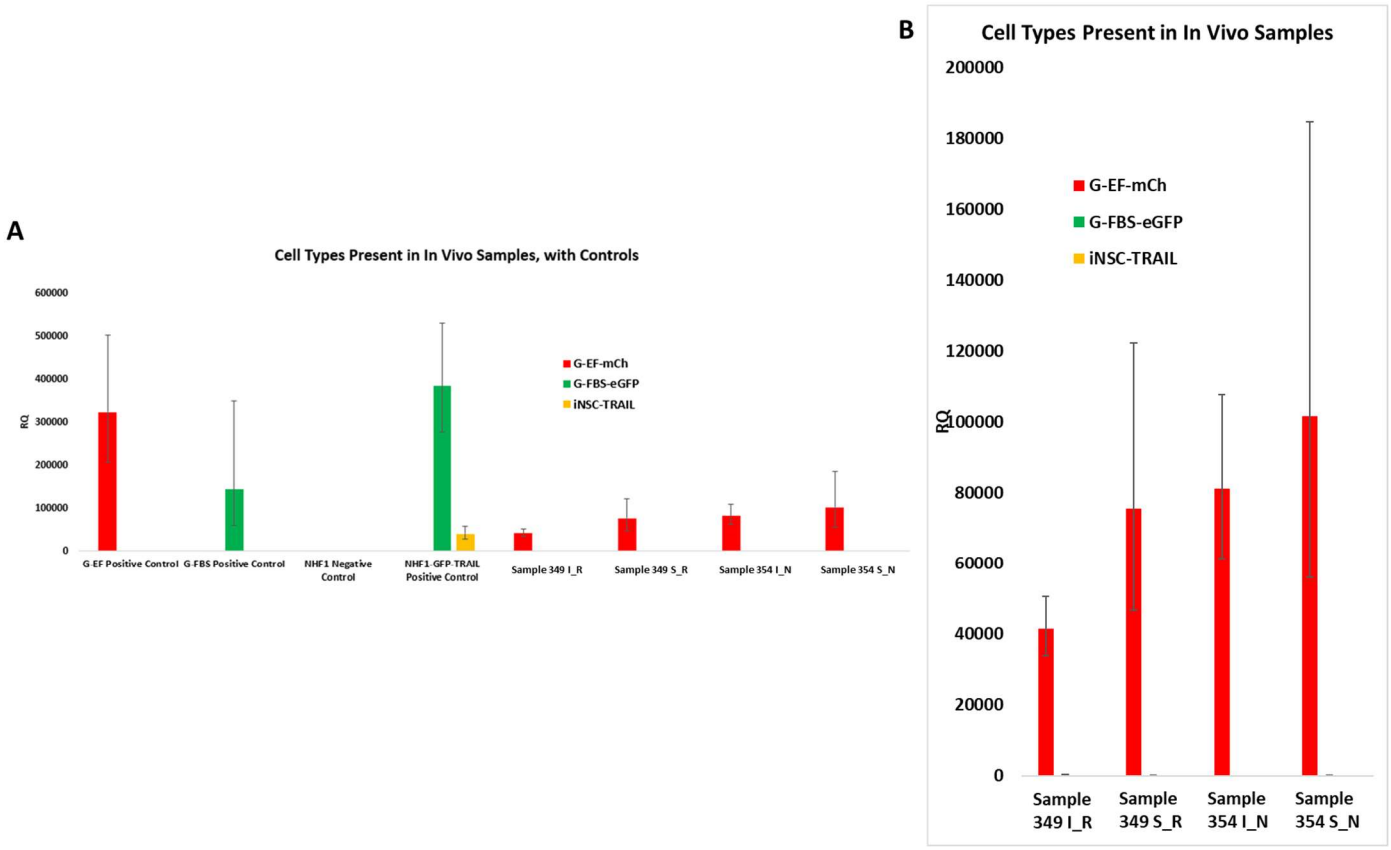

Figure S1: qPCR of tumor tissue grown *in vivo* and dissected from cryosections in accordance with our RNA sequencing procedure. Tumor samples were taken from either the solid or invasive cell populations in untreated or treated/recurrent samples. Tumors were initially implanted with a mix of red G-EF and green G-FBS cells, but PCR confirms that by time of death only the red G-EF cells remain. A) displays positive and negative controls alongside *in vivo* tumor samples; B) displays tumor samples with a broader y-axis to more effectively show the lack of green signal from G-FBS cells.

Figure S2:

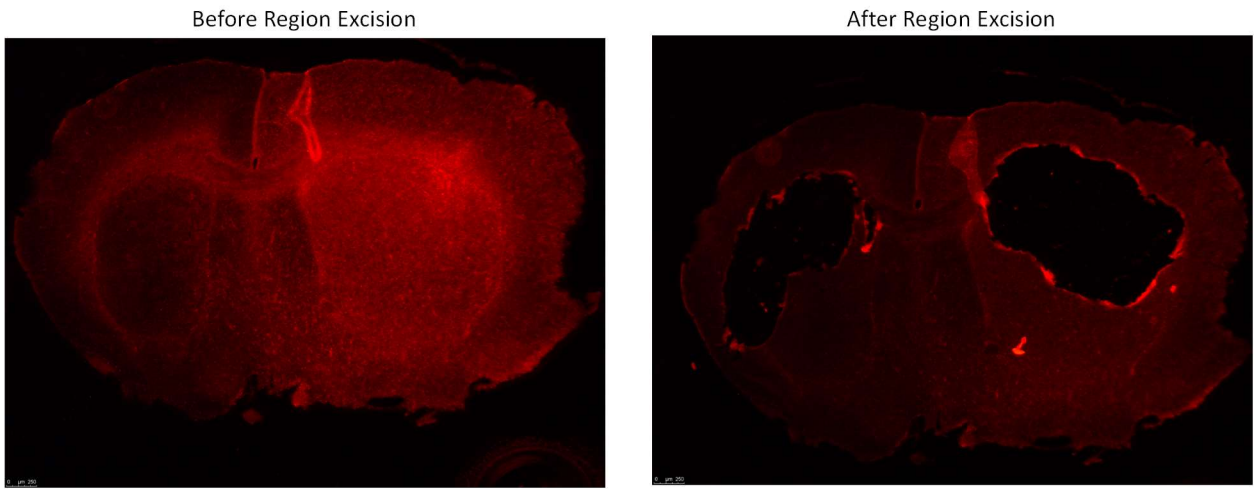

Figure S2: Example of a 60 µm-thick cryosection of tumor-bearing brain before and after excision of solid (right) and invasive (left) tumor regions for RNA isolation.

Figure S3:

A

Sample #	ID	Treated?	RIN	Qubit (ng/uL)
1	354_S	N	8.6	28.9
2	354_I	N	8	25.7
3	339_S	N	8.6	61
4	339_I	N	7.3	22.6
5	342_S	N	7.5	46.8
6	342_I	N	7.5	17.7
7	377_S	Y	8.6	13.7
8	377_I	Y	7.8	31.8
9	349_S	Y	8	18.9
10	349_I	Y	8	24.5
11	373_S	Y	8.3	17.6
12	373_I	Y	9.4	24.3

B

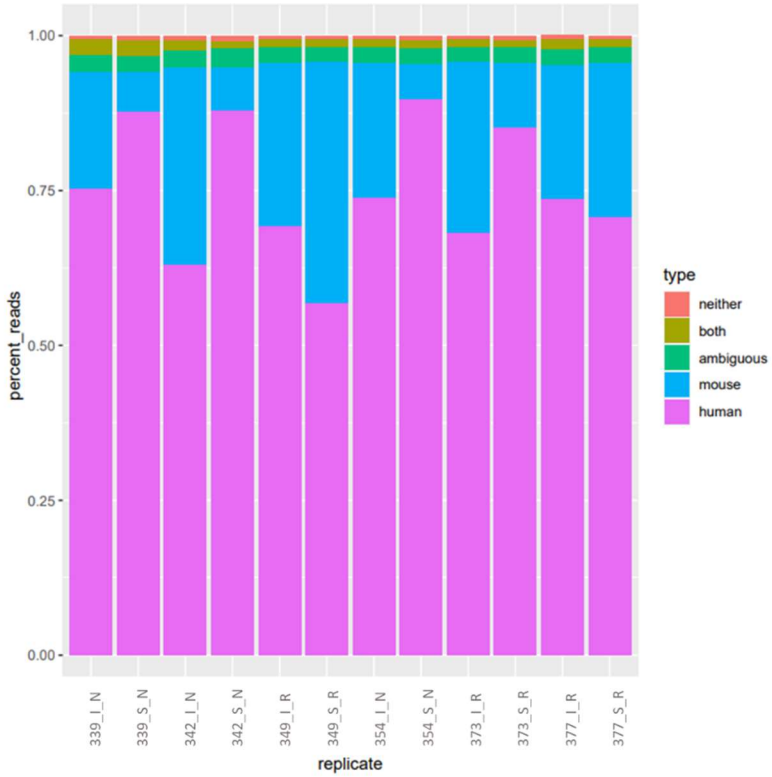

Figure S3: RNAseq Quality Control. A) Quantification of RNA quality (RIN) for samples used in mRNA-seq analysis. B) RNAseq analysis human vs mouse reads per sample

Figure S4

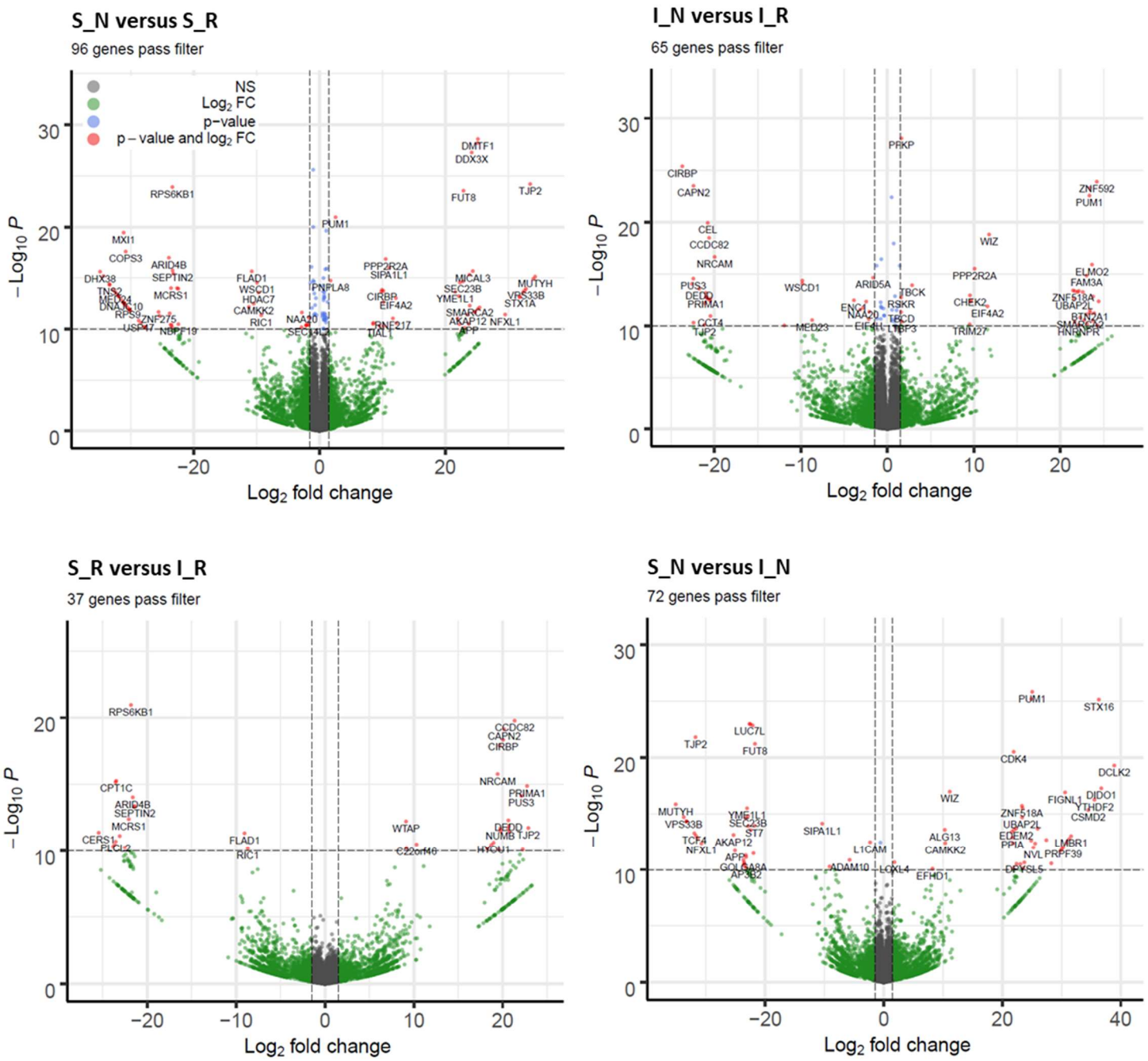

Figure S4: Volcano plots displaying gene expression profiles in pairwise comparison between S_N vs S_R, I_N vs I_R, S_N vs I_N, and S_R vs I_R.

Figure S5

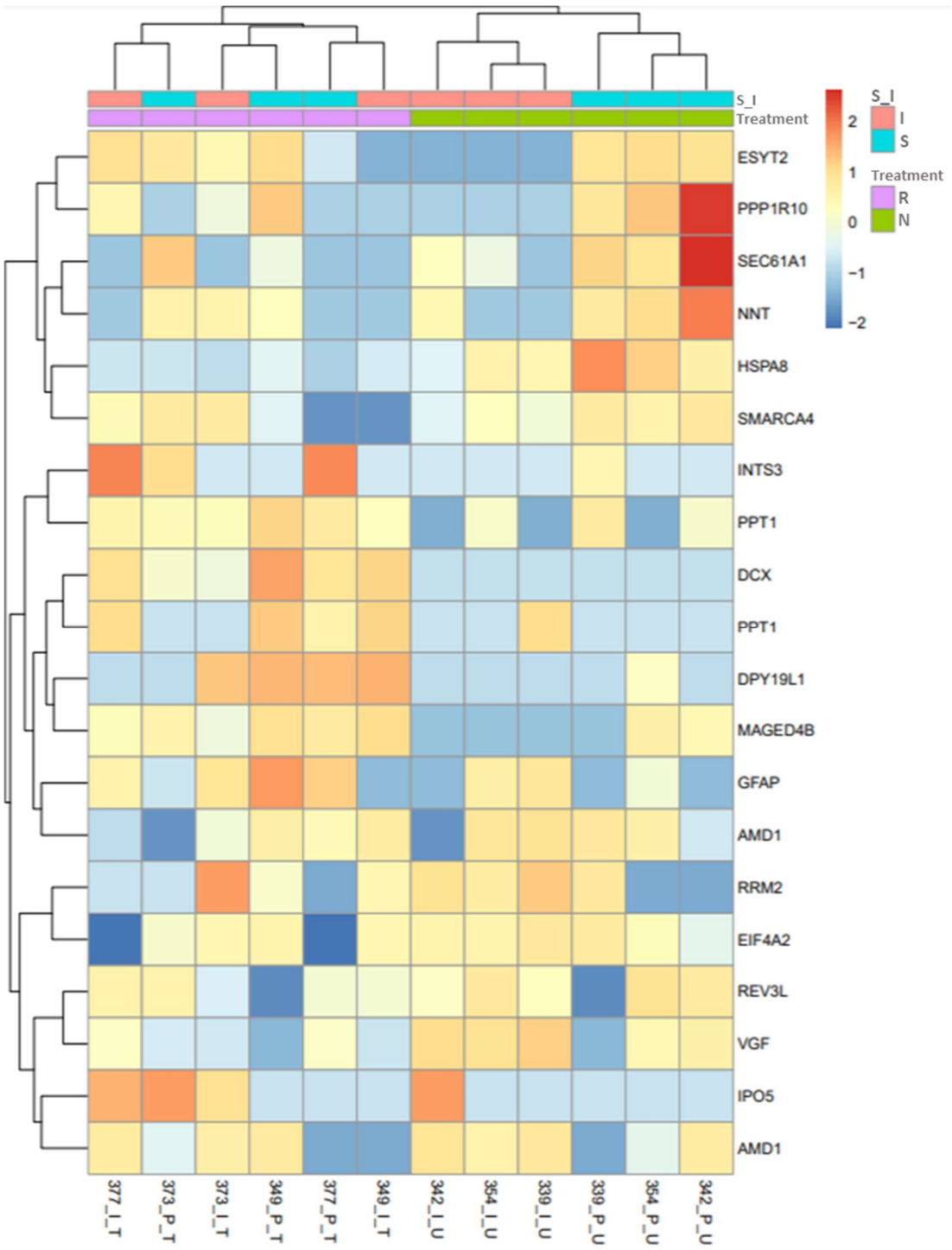

Figure S5: Unsupervised hierarchical clustering of 20 most variable genes

Figure S6:

Upregulated in all six treated samples		Downregulated in all six treated samples		Upregulated in all six primary samples		Downregulated in all six primary samples	
AARS2	RBBP5	ACP1	LAMTOR5	ADCY7		ABCB7	
ACSS3	RBCK1	ADNP2	LMNA	AURKA		ANKHD1	
ADCY6	RBM4B	ALKBH2	M6PR	C22orf46		APP	
ADGRG1	RFX1	ANK2	MAGED1	CSMD2		CELF2	
AGAP1	RIC8B	AP2A2	MAN1B1	DCAF11		CEP78	
ALDH7A1	SF1	ARHGAP21	MAPK3	DCLK2		CTNNB1	
APBA3	SLC11A2	ARID5A	MBNL2	DDX3X		DIS3L2	
APC2	SLC12A9	ARL4C	MECP2	DIDO1		DNAJC16	
ARID5B	SLC26A11	ARMCX6	MED24	FAM122B		GPS1	
ARL10	SLX1B	ARPP19	MTMR2	FIGNL1		LTBP1	
ASIC4	SMARCA2	ASCC3	MXI1	LMBR1		MARK1	
ASNS	SMARCA4	ASPH	MYB	NVL		POU2F1	
ATF6B	SMYD2	ATRN	NAA20	PRPF39		PRIMA1	
ATXN2L	SNAPC3	ATXN1	NISCH	SMARCA4		RAD54L	
BCAN	SNX1	BAP1	NUDCD3	STX16		SCN1A	
BFAR	SOBP	BCKDHB	PAPOLG	SYNE1		ST7	
BID	SOGA1	C1orf198	PARP2	TEX264		SUMF2	
BRD3	SPRY4	CALD1	PCBP2	YTHDF2			
BTN2A1	SPTAN1	CASP3	PDIA5				
C22orf39	SRGAP2	CAST	PHB2				
C22orf46	SRGAP2B	CCDC25	PHYHIP				
CA14	SRRM2	CENPU	PIGG				
CCNF	SRSF1	CHCHD3	PLCD3				
CEP152	ST8SIA1	CHL1	POLR1D				
CHEK2	ST8SIA5	CIZ1	POLR2G				
CHN1	TAF1A	CLPTM1	PPIE				
CPAMD8	TBCD	CNBP	PTAR1				
CTNND1	TBCK	COPS3	PWP1				
DBF4B	TIAL1	CSDE1	RGS2				
DDX17	TJP2	CUTC	RINT1				
DIAPH1	TOR1AIP2	DBN1	RNASEH2B				
DPYSL5	TPP2	DCAF7	RNASEH2C				
DTX3	TRIM7	DDX18	ROM1				
DUXAP9	TRMT2A	DDX39B	RPL23AP82				
EIF4A2	TROAP	DHX38	RPS9				
ESD	TTF2	DMAC2	SEC14L2				
FAM219B	UBN2	DNAJC10	SEPHS1				
FRY	UBP1	DNM3	SESTD1				
GALNT16	USP20	DST	SMAP1				
GAS2L3	YEATS2	EIF2B1	SMARCD2				
GBX2	YIPF5	EIF4E3	SNRNP27				
GTF2IP1	YLPM1	EIF4H	SOCS3				
GTF2IP20	ZDHHC3	EMG1	SP3				
H1-9P	ZFHX2	ENDOD1	SPRY1				
HPS4	ZNF717	EPB41L3	SPTSSA				
HR	ZNF800	ERI2	SRI				
IKBKB	ZNF821	FAM160B1	SRSF5				
IRF2BP2	ZWINT	FASTK	SSBP1				
JRK		FCRLA	STAU2				
KDM4A		FIP1L1	STK17A				
KIF18B		GASK1A	SYNJ2				
KMT2A		GLCE	TAF5L				
LTBP3		GPC1	TAGLN2				
LUC7L		GTPBP2	TCEAL8				
MAGED4B		GYG1	TECPR2				
MAGI2		HBS1L	TIA1				
MCCC2		HECW2	TM4SF1				
MEIS3		HMGA2	TMEM158				
MON1A		HNRNPC	TNS2				
NACA		HNRNPL	TTC19				
NSUN5P1		HOXA4	TTC32				
NUP43		IFT57	UBTD1				
PABPC1L		INF2	UCHL1				
PASK		ING3	USP46				
PFKP		INTS10	USP47				
PIF1		ITGAE	VPS29				
POLH		KCTD18	WDR45B				
PPP2R2A		KMT2E	WSCD1				
PUM1		KRR1	XK				
PUS1		LAMP1	YKT6				
			ZNF160				
			ZNF280D				

Figure S6: Genes up- or down-regulated in all six treated/recurrent tumor samples vs untreated, or in all six solid/primary tumor samples vs invasive; p-value threshold for each sample < 0.001

Figure S7:

S_N versus I_N

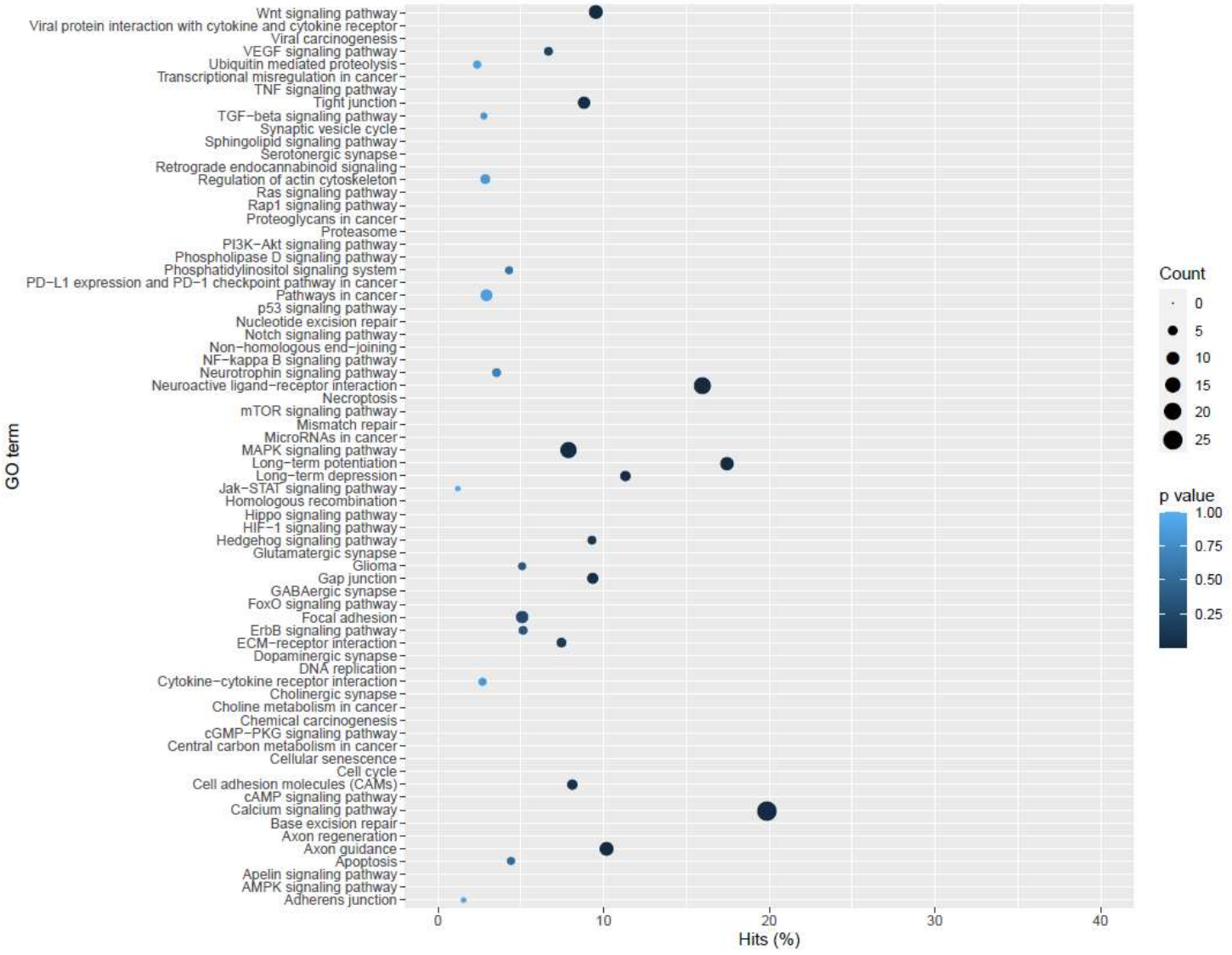

S_N versus S_R

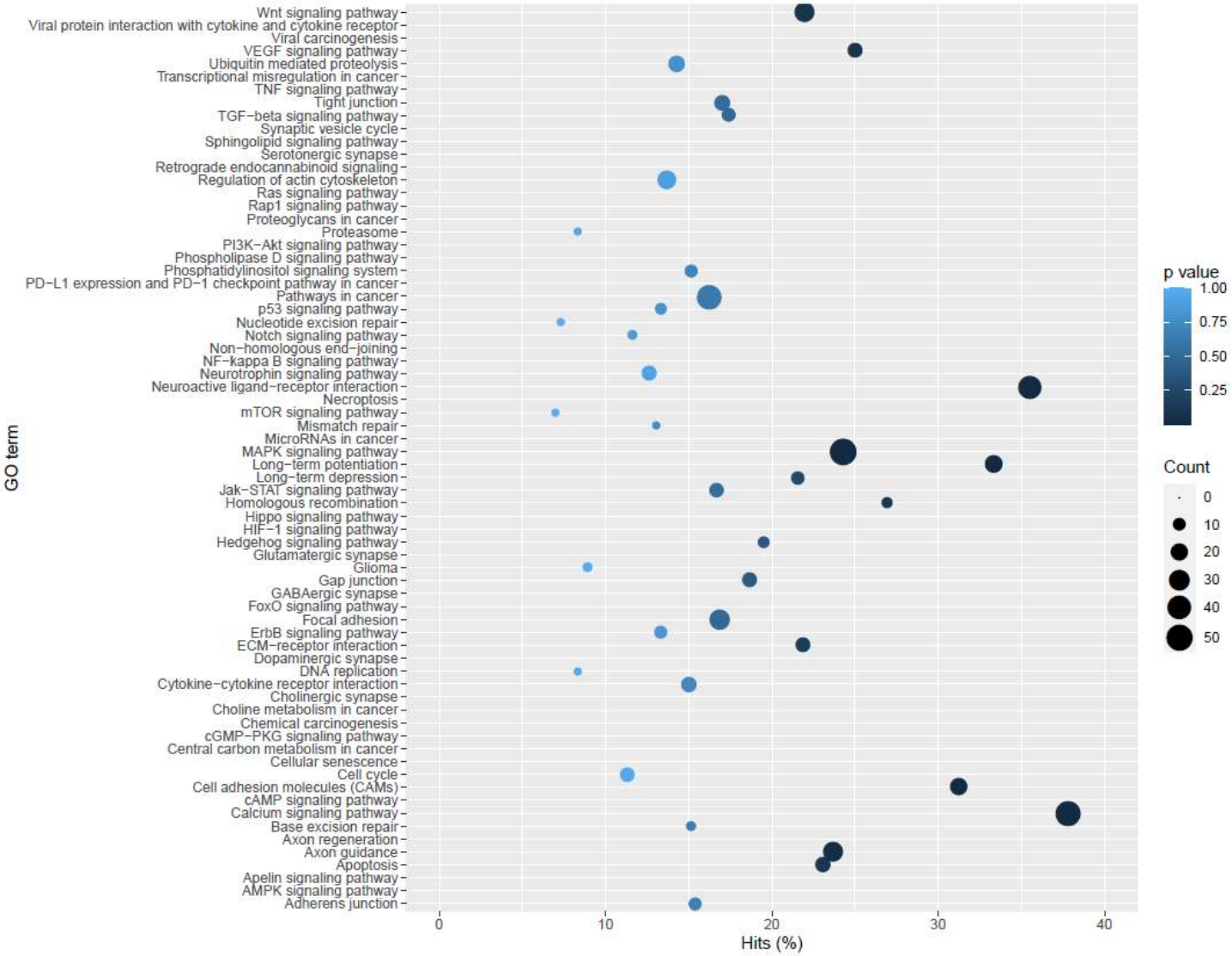
Wnt signaling pathway
Viral protein interaction with cytokine and cytokine receptor
Viral carcinogenesis
VEGF signaling pathway
Ubiquitin mediated proteolysis
Transcriptional misregulation in cancer
TNF signaling pathway
Tight junction
TGF−beta signaling pathway
Synaptic vesicle cycle
Sphingolipid signaling pathway
Serotonergic synapse
Retrograde endocannabinoid signaling
Regulation of actin cytoskeleton
Ras signaling pathway
Rap1 signaling pathway
Proteoglycans in cancer
Proteasome
PI3K−Akt signaling pathway
Phospholipase D signaling pathway
Phosphatidylinositol signaling system
PD−L1 expression and PD−1 checkpoint pathway in cancer
Pathways in cancer
p53 signaling pathway
Nucleotide excision repair
Notch signaling pathway
Non−homologous end−joining
NF−kappa B signaling pathway
Neurotrophin signaling pathway
Neuroactive ligand−receptor interaction
Necroptosis
mTOR signaling pathway
Mismatch repair
MicroRNAs in cancer
MAPK signaling pathway
Long−term potentiation
Long−term depression
Jak−STAT signaling pathway
Homologous recombination
Hippo signaling pathway
HIF−1 signaling pathway
Hedgehog signaling pathway
Glutamatergic synapse
Glioma
Gap junction
GABAergic synapse
FoxO signaling pathway
Focal adhesion
ErbB signaling pathway
ECM−receptor interaction
Dopaminergic synapse
DNA replication
Cytokine−cytokine receptor interaction
Cholinergic synapse
Choline metabolism in cancer
Chemical carcinogenesis
cGMP−PKG signaling pathway
Central carbon metabolism in cancer
Cellular senescence
Cell cycle
Cell adhesion molecules (CAMs)
cAMP signaling pathway
Calcium signaling pathway
Base excision repair
Axon regeneration
Axon guidance
Apoptosis
Apelin signaling pathway
AMPK signaling pathway
Adherens junction
GO term
0
10
20
30
40
Hits (%)
p value
1.00
0.75
0.50
0.25
Count
0
10
20
30
40
50

I_N versus I_R

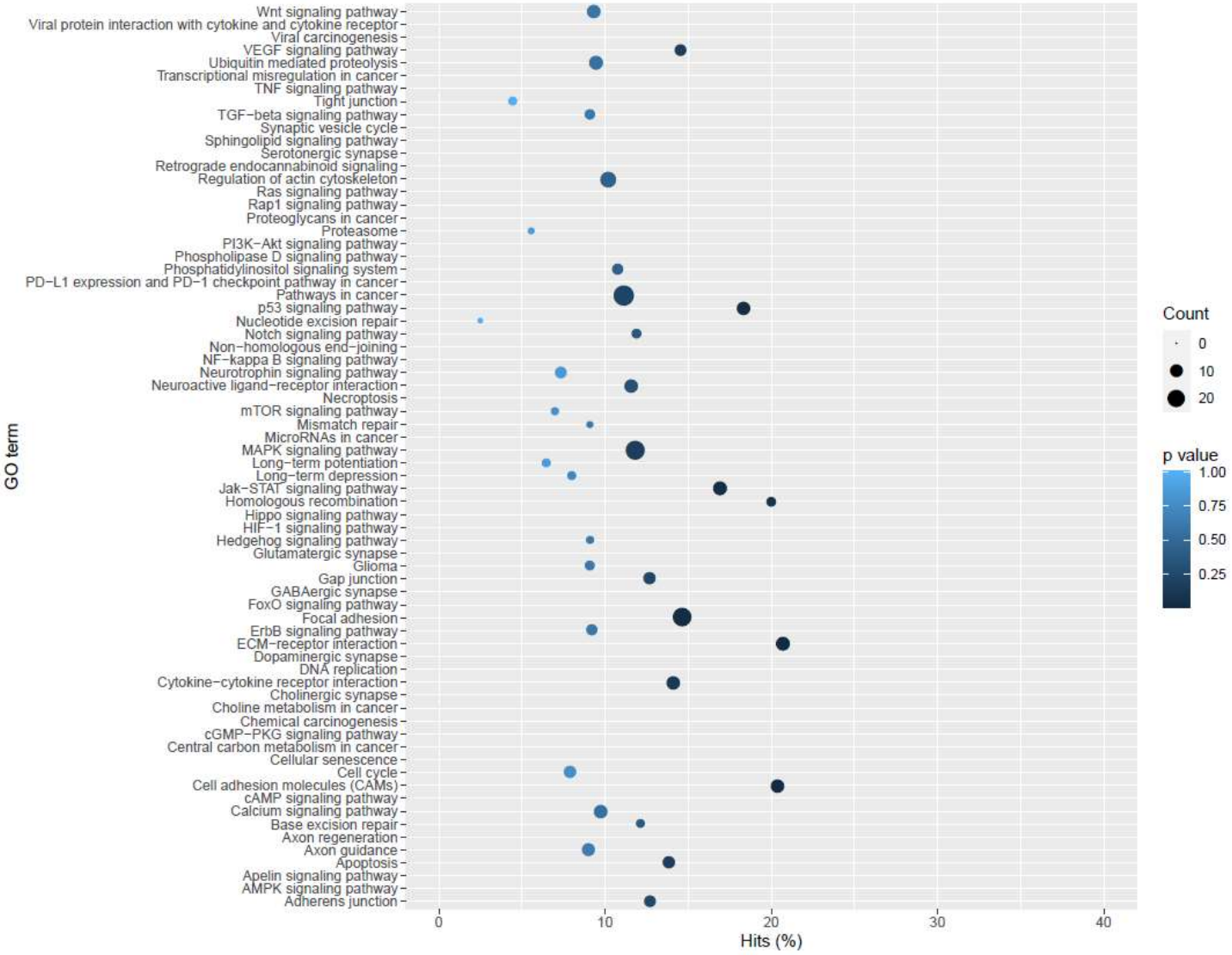
Wnt signaling pathway
Viral protein interaction with cytokine and cytokine receptor
Viral carcinogenesis
VEGF signaling pathway
Ubiquitin mediated proteolysis
Transcriptional misregulation in cancer
TNF signaling pathway
Tight junction
TGF−beta signaling pathway
Synaptic vesicle cycle
Sphingolipid signaling pathway
Serotonergic synapse
Retrograde endocannabinoid signaling
Regulation of actin cytoskeleton
Ras signaling pathway
Rap1 signaling pathway
Proteoglycans in cancer
Proteasome
PI3K−Akt signaling pathway
Phospholipase D signaling pathway
Phosphatidylinositol signaling system
PD−L1 expression and PD−1 checkpoint pathway in cancer
Pathways in cancer
p53 signaling pathway
Nucleotide excision repair
Notch signaling pathway
Non−homologous end−joining
NF−kappa B signaling pathway
Neurotrophin signaling pathway
Neuroactive ligand−receptor interaction
Necroptosis
mTOR signaling pathway
Mismatch repair
MicroRNAs in cancer
MAPK signaling pathway
Long−term potentiation
Long−term depression
Jak−STAT signaling pathway
Homologous recombination
Hippo signaling pathway
HIF−1 signaling pathway
Hedgehog signaling pathway
Glutamatergic synapse
Glioma
Gap junction
GABAergic synapse
FoxO signaling pathway
Focal adhesion
ErbB signaling pathway
ECM−receptor interaction
Dopaminergic synapse
DNA replication
Cytokine−cytokine receptor interaction
Cholinergic synapse
Choline metabolism in cancer
Chemical carcinogenesis
cGMP−PKG signaling pathway
Central carbon metabolism in cancer
Cellular senescence
Cell cycle
Cell adhesion molecules (CAMs)
cAMP signaling pathway
Calcium signaling pathway
Base excision repair
Axon regeneration
Axon guidance
Apoptosis
Apelin signaling pathway
AMPK signaling pathway
Adherens junction
GO term
0
10
20
30
40
Hits (%)
Count
0
10
20
p value
1.00
0.75
0.50
0.25

S_R versus I_R

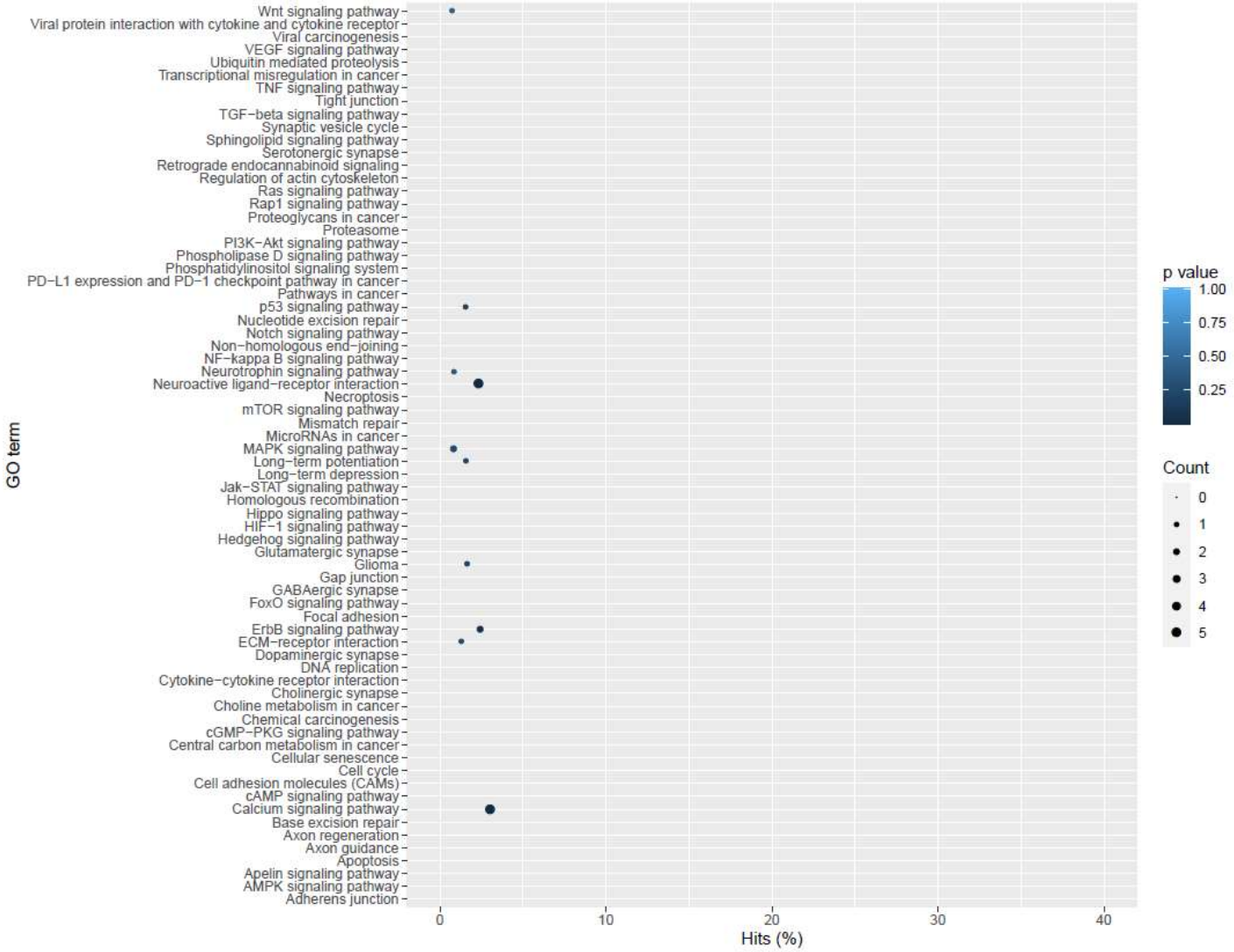

Figure S7: Plots of pairwise comparison of KEGG pathway expression changes. Each pathway is named row-by-row on the left of each plot. Circle size = number of changed genes per pathway; circle position = percent of changed genes per pathway; circle color = overall significance of pathway changes.

Figure S8:

Figure S8: Confirmation of spread of Evans Blue solution after ICV injection into the left lateral ventricle at (1.1, 0, 2.5) from Bregma. Brain dissected t = 2 minutes after injection.

Figure S9:

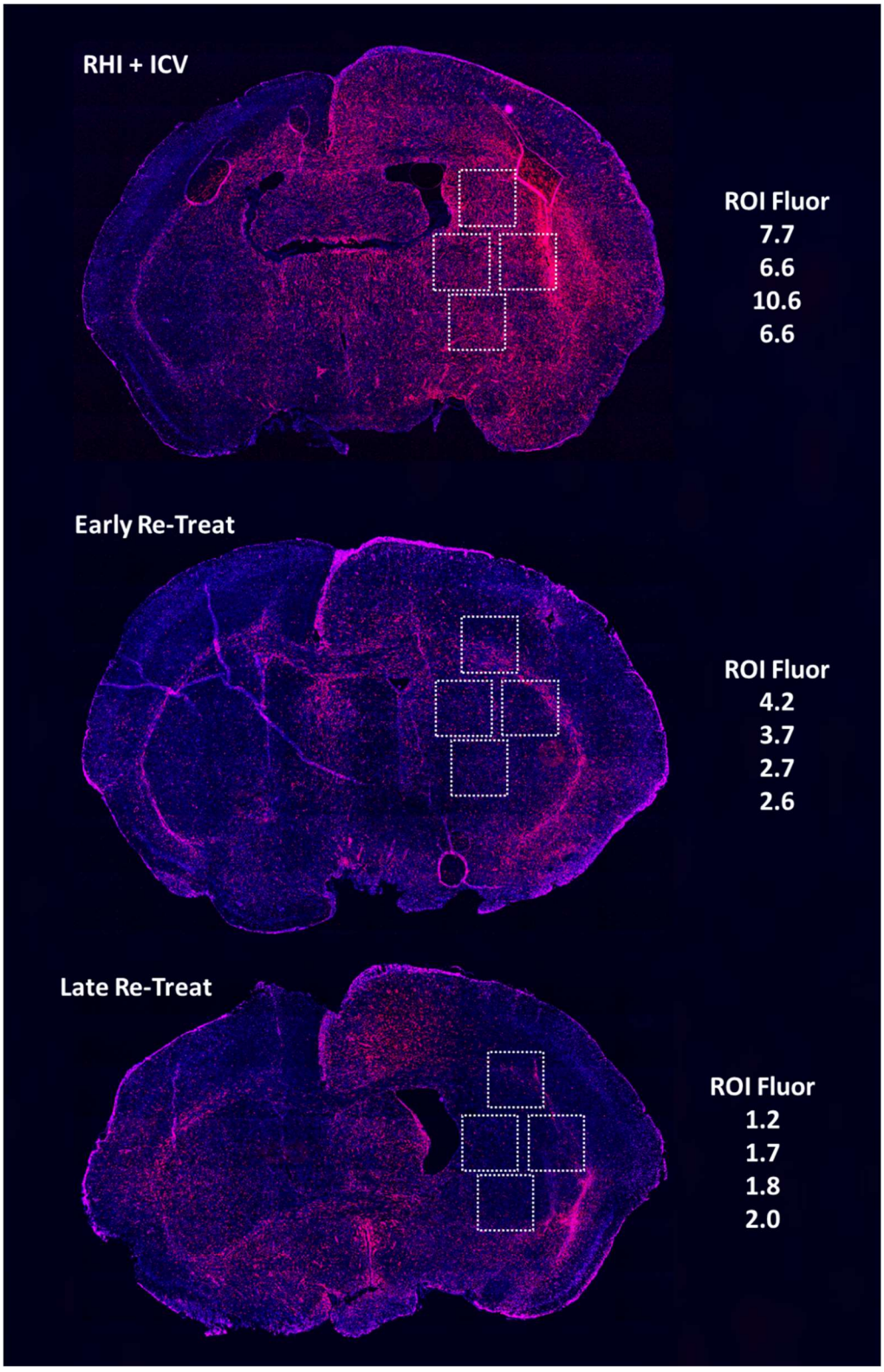

Figure S9: Fluorescence images of cryo-sectioned coronal brain sections shown in Figure 4D. Tumor burden along RHI site was measured via background-subtracted red fluorescence intensity quantification in fluorescence cryosections. n = 4 representative areas of 1mm^2 each are outlined in white with fluorescence intensities displayed on the right.

Figure S10:

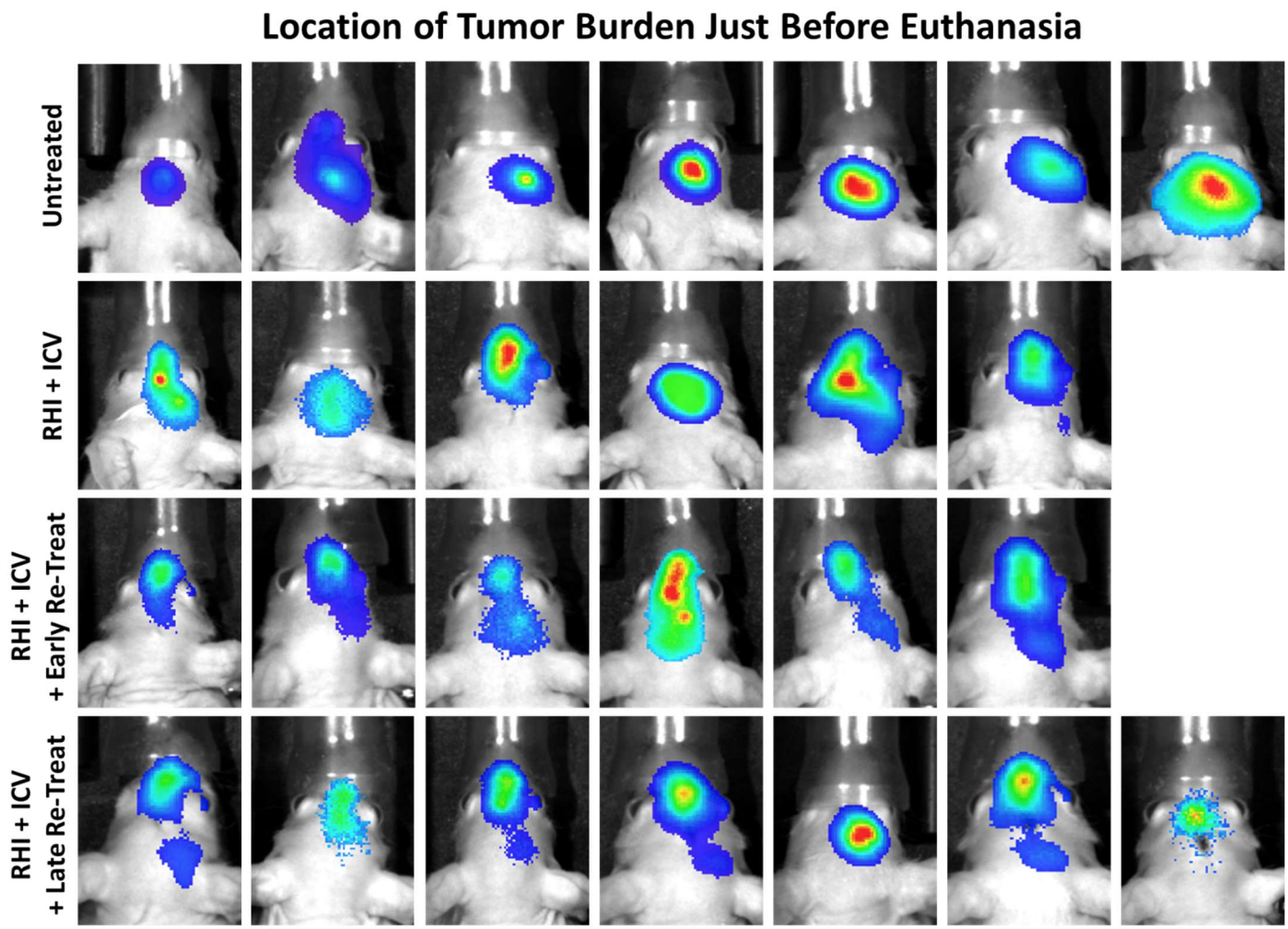

Figure S10: Additional examples of tumor regrowth in anterior and posterior regions of the brain as introduced in Figure 4D. After single treatment, regrowth occurs near the original implant site, but after early or late re-treatment, tumor re-growth more frequently occurs in anterior and posterior regions.

Figure S11:

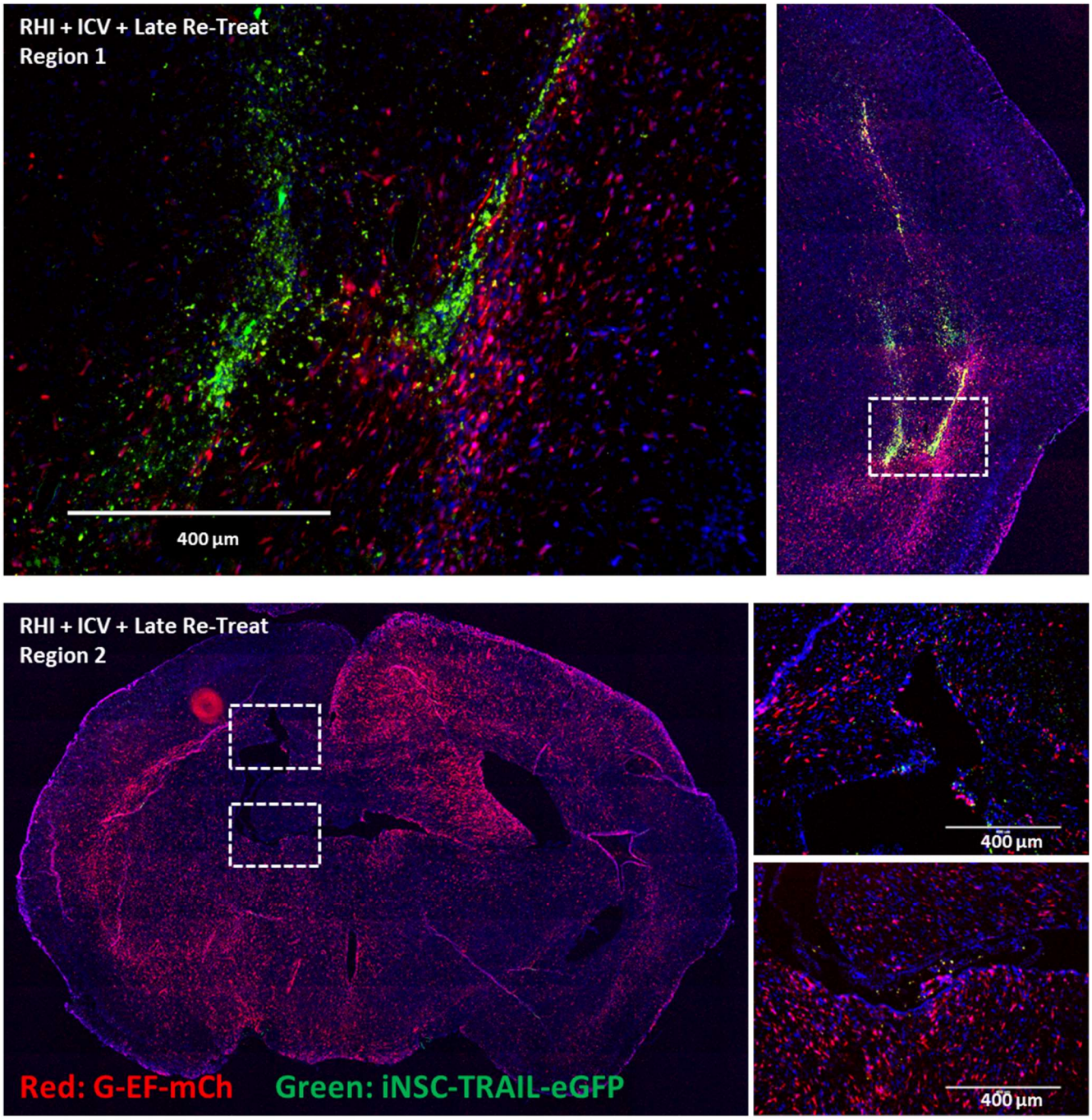

Figure S11: Higher magnification images and additional regions of brain at study endpoints after RHI + ICV + Late Re-Treatment with iNSC-TRAIL. iNSC-TRAIL cells are still alive within the brain of this animal.